



# 1        **Characterizing the marine iodine cycle and its relationship to** 2        **ocean deoxygenation in an Earth System model**

3        Keyi Cheng<sup>1</sup>, Andy Ridgwell<sup>2</sup>, Dalton S. Hardisty<sup>1</sup>

4        <sup>1</sup>Department of Earth and Environmental Sciences, Michigan State University, East Lansing, 48823, USA

5        <sup>2</sup>Department of Earth and Planetary Sciences, University of California Riverside, Riverside, 92521, USA

6        *Correspondence* to: Keyi Cheng (chengkey@msu.edu)

7        **Abstract.** Iodine abundance in marine carbonates (as an elemental ratio with calcium – I:Ca) is of broad interest as a  
8        proxy for local/regional ocean redox. This connection arises because the speciation of iodine in seawater—in terms  
9        of the balance between iodate ( $\text{IO}_3^-$ ) and iodide ( $\text{I}^-$ )—is sensitive to the prevalence of oxic vs. anoxic conditions.  
10        However, although I:Ca ratios are being increasingly commonly measured in ancient carbonate samples, a fully  
11        quantitative interpretation of this proxy is hindered by the scarcity of a mechanistic and quantitative framework for  
12        the marine iodine cycle and its sensitivity to the extent and intensity of ocean deoxygenation. Here we present and  
13        evaluate a representation of marine iodine cycling embedded in an Earth system model ('cGENIE') against both  
14        modern and paleo observations. In this, we account for  $\text{IO}_3^-$  uptake and reduction by primary producers, the  
15        occurrence of ambient  $\text{IO}_3^-$  reduction in the water column, plus the re-oxidation of  $\text{I}^-$  to  $\text{IO}_3^-$ . We develop and test a  
16        variety of different mechanistic relationships between  $\text{IO}_3^-$  and  $\text{I}^-$  against an updated compilation of observed  
17        dissolved  $\text{IO}_3^-$  and  $\text{I}^-$  concentrations in the present-day ocean. In optimizing the parameters controlling previously  
18        proposed mechanisms behind marine iodine cycling, we find that we can obtain broad matches to observed iodine  
19        speciation gradients in zonal surface distribution, depth profiles, and oxygen deficient zones (ODZs). We also  
20        identify alternative, equally well performing mechanisms which assume a more explicit mechanistic link between  
21        iodine transformation and environment. This mechanistic ambiguity highlights the need for more process-based  
22        studies on modern marine iodine cycling. Finally, because our ultimate motivation is to further our ability to  
23        reconstruct ocean oxygenation in the geological past, we conducted 'plausibility tests' of our various different model  
24        schemes against available I:Ca measurements made on Cretaceous carbonates – a time of substantially depleted  
25        ocean oxygen availability compared to modern and hence a strong test of our model. Overall, the simultaneous  
26        broad match we can achieve between modelled iodine speciation and modern observations, and between forward-  
27        proxy modelled I:Ca and geological elemental ratios supports the application of our Earth system modelling in  
28        simulating the marine iodine cycle to help interpret and constrain the redox evolution of past oceans.

## 29        **1. Introduction**

30        Dissolved Iodine (I) in seawater is redox sensitive and as such, a potential invaluable delineator of past ocean  
31        deoxygenation. This arises directly from: (1) observations that the oxidized iodate ( $\text{IO}_3^-$ ) is reduced to iodide ( $\text{I}^-$ ) under  
32        low oxygen conditions, and (2) that  $\text{IO}_3^-$  in seawater is incorporated into carbonate lattice during precipitation in  
33        proportion to its seawater abundance (whilst  $\text{I}^-$  is not) (Lu et al., 2010; Podder et al., 2017; Kerisit et al., 2018; Zhang  
34        et al., 2013; Hashim et al., 2022). Hence, past ocean  $\text{IO}_3^-$  concentrations can be recorded in coeval carbonates as I:Ca

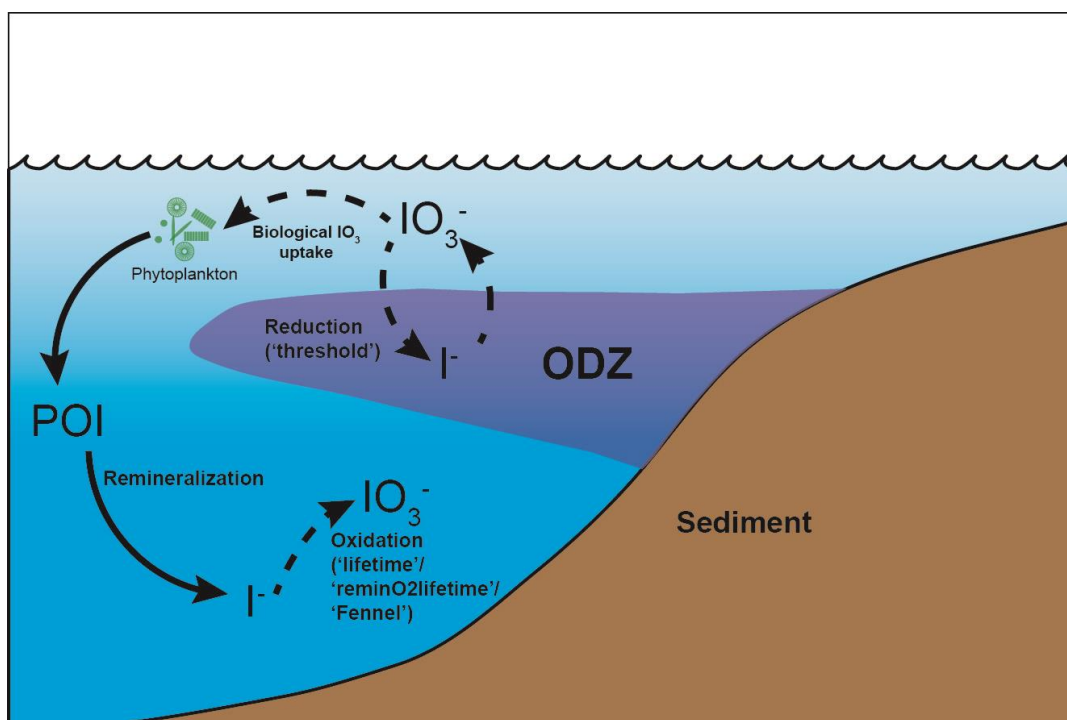


35 ratios, with the potential of carbonate I:Ca to reflect the redox variation of the ancient seawater (Lu et al., 2010).  
36 Indeed, the I:Ca ratio in marine carbonates is already widely applied as a paleoredox proxy, with studies employing it  
37 to explore the [O<sub>2</sub>] variation throughout much of Earth history, from the Archean and through the Cenozoic (Lu et al.,  
38 2010; Hardisty et al., 2014; Zhou et al., 2015; Lu et al., 2016; Edwards et al., 2018; Lu et al., 2018; Bowman et al.,  
39 2020; Pohl et al., 2021; Wei et al., 2021; Ding et al., 2022; Shang et al., 2019; Liu et al., 2020; Fang et al., 2022;  
40 Uahengo et al., 2020; Yu et al., 2022; Tang et al., 2023). The potential for I:Ca to generate critical insights into how  
41 the oxygenation of the ocean has evolve through time, as well as the causes and biological/ecological consequences  
42 of this, requires that we have an adequate understanding, not only of carbonate IO<sub>3</sub><sup>-</sup> incorporation, but of the marine  
43 iodine cycle in general.

44 Progress has been made towards understanding the marine iodine cycle in the past decades. Iodine has a long  
45 residence time (~300 kyr; Broecker and Peng, 1983), making its concentration among the global ocean relatively  
46 constant around 500nM (Elderfield and Truesdale, 1980; Truesdale et al., 2000; Chance et al., 2014). Although the  
47 total concentration is relatively invariant, the two most abundant species of dissolved iodine in the ocean, IO<sub>3</sub><sup>-</sup> and  
48 iodide I<sup>-</sup>, vary relative to each other depending on the environment. Today, IO<sub>3</sub><sup>-</sup> is generally the dominant iodine  
49 species in oxygenated regions of the ocean, representing total iodine nearly quantitatively below the euphotic zone.  
50 Within the euphotic zone, I<sup>-</sup> occurs and generally increases in association with release during phytoplankton growth  
51 and senescence (Hepach et al., 2020). Iodide is also more abundant in oxygen deficient zones (ODZ) – often but not  
52 always quantitatively so (Truesdale et al., 2000; Rue et al., 1997; Cutter et al., 2018; Moriyasu et al., 2020; Farrenkopf  
53 and Luther, 2002; Wong and Brewer, 1977; Truesdale et al., 2013; Rapp et al., 2020, 2019). Respectively, within the  
54 ODZ, IO<sub>3</sub><sup>-</sup> is reduced to I<sup>-</sup> and hence has low concentrations (Rue et al., 1997; Farrenkopf et al., 1997; Moriyasu et al.,  
55 2020; Rapp et al., 2019, 2020).

56 Although generally depleted in low-[O<sub>2</sub>] settings, the causal spatial relationship between seawater [O<sub>2</sub>] and  
57 [IO<sub>3</sub><sup>-</sup>] is not simple and is currently not well understood. Recently published observations from global oxygen deficient  
58 zones (ODZ) reveals that the relationship between dissolved [O<sub>2</sub>] and [IO<sub>3</sub><sup>-</sup>] is not linear, but instead it is possible that  
59 there is a certain [O<sub>2</sub>] or related redox threshold triggering IO<sub>3</sub><sup>-</sup> reduction (Cutter et al., 2018; Moriyasu et al., 2020;  
60 Farrenkopf and Luther, 2002; Rue et al., 1997; Chapman, 1983). Dissimilatory IO<sub>3</sub><sup>-</sup> reducing bacteria, as well as  
61 abiotic reduction with sulfide and dissolved Fe, have been identified within ODZs (Farrenkopf et al., 1997; Councill  
62 et al., 1997; Jiang et al., 2023). In addition, slow oxidation-reduction kinetics (Tsunogai, 1971; Hardisty et al., 2020;  
63 Schnur et al., 2024) imply the likelihood that *in situ* iodine signals could be integrated across large-scale physical  
64 oceanography processes – including ocean currents and mixing between water masses (Hardisty et al., 2021), and  
65 meaning that iodine species reflect regional rather than local redox conditions (Lu et al., 2020b). Non-redox related  
66 processes, such as phytoplankton-mediated IO<sub>3</sub><sup>-</sup> reduction and organic matter remineralization also exerts controls on  
67 iodine speciation in the water column (Fig. 1; Elderfield and Truesdale, 1980; Wong et al., 1985; Luther and Campbell,  
68 1991; Hepach et al., 2020). Therefore, it is difficult to infer water column redox simply based on iodine speciation  
69 without considering these physical and biological effects.

70



71 **Figure 1: The iodine cycle in marine oxygen deficient zones (ODZ) in cGENIE. The oxidation-reduction options**  
 72 **(‘threshold’ and ‘lifetime’/ ‘reminO2lifetime’/ ‘Fennel’)** are described in Section 2.2 and Table 1. **Dashed**  
 73 **arrows indicate variable processes during ensemble simulations. Note that the POI export is controlled by**  
 74 **temperature (TDEP).**  
 75

76

77 Apart from the uncertainties associates with  $\text{IO}_3^-$  reduction, it is notable that the oxidants responsible for  $\text{IO}_3^-$   
 78 formation during the re-oxidation  $\text{I}^-$  are currently unknown, only that it is unlikely to be  $\text{O}_2$ , which is not  
 79 thermodynamically favorable to oxidize iodine (Luther et al., 1995). A recent thermodynamic review indicates that  
 80 the reactive oxygen species (ROS) such as hydrogen peroxide and OH radicals can fully oxidize  $\text{I}^-$  to  $\text{IO}_3^-$ . Iodide  
 81 oxidation to  $\text{IO}_3^-$  is a 6-electron transfer and other ROS, such as superoxide, are only thermodynamically favorable to  
 82 catalyze partial oxidation to intermediates (Luther, 2023). These ROS species have heterogenous distributions and  
 83 ambient ocean concentrations that are typically relatively low compared to iodine, supporting the likelihood of  
 84 temporally or spatially isolated high  $\text{I}^-$  oxidation rates despite of overall extremely slow rates (Schnur et al., 2024).  
 85 Additional support for spatially or temporally heterogenous  $\text{I}^-$  oxidation rates comes from recent experimental  
 86 observations of  $\text{IO}_3^-$  production from  $\text{I}^-$  in nitrifying cultures (Hughes et al., 2021). Nitrification rates vary globally,  
 87 with the highest values occurring in ODZs and the dissolved chlorophyll maximum (summarized in Table 2 of Hughes  
 88 et al., 2021). Regardless, nitrification or other specific mechanisms have yet to be linked directly to  $\text{I}^-$  oxidation under  
 89 normal marine conditions, leaving open the question of rates and locations of  $\text{I}^-$  oxidation.

90 Given the prevailing uncertainty in the mechanisms governing the marine iodine cycle mentioned above, and  
 91 in conjunction with I:Ca being a relatively new proxy, it is perhaps not surprising that few attempts have been made



92 to model the marine iodine cycle. In a recent publication, a model was developed to simulate modern ocean surface I  
93 distributions, with the aim of being able to improve tropospheric ozone models (Wadley et al., 2020). This particular  
94 model was based around a relatively high horizontal ocean resolution (1° grid size) with a 3-layer vertical water  
95 column. Iodine biogeochemical cycling was coupled with the nitrogen cycle, with the surface I distribution sensitive  
96 to biological and hydrological factors including primary productivity, I:C ratio, oxidation, mixed layer depth,  
97 advection, and freshwater flux. Because the Wadley et al., (2020) model was specifically focused on near-surface  
98 processes within the upper 500 m, it did not consider processes occurring within ODZs and hence is not directly  
99 applicable to questions concerning the controls on I:Ca ratios. In contrast, a second model-based study deliberately  
100 targeted paleoceanographic questions and incorporated an iodine cycle including redox-controlled biogeochemical  
101 reactions into the ‘cGENIE’ Earth system model (Lu et al., 2018). The advantage for paleo studies afforded by this  
102 particular approach is that the cGENIE model can take into account different continental configurations, non-modern  
103 atmospheric composition (pO<sub>2</sub>, pCO<sub>2</sub>), and other boundary conditions that may have differed on ancient Earth relative  
104 to today (Ridgwell et al., 2007; Reinhard et al., 2016; Boscolo-Galazzo et al., 2021; Rimmelzwaal et al., 2019; Pohl  
105 et al., 2022; Reinhard and Planavsky, 2022).

106 Despite a growing understanding of I:Ca variations through geologic time, it remains challenging to  
107 determine mechanisms driving spatiotemporal marine [IO<sub>3</sub><sup>-</sup>] and the degree that these are linked to seawater oxygen.  
108 Hence, the proxy is qualitative or semi-quantitative. Here, we calibrate the iodine cycle within the cGENIE Earth  
109 System model to provide a mechanistic framework for interpreting ancient I:Ca variations. In this study, we build on  
110 the work of Lu et al., 2018 and further develop and test a series of new potential parameterizations for water column  
111 iodine oxidation, reduction, cellular uptake, and release during remineralization. We also developed 3 criteria for  
112 assessing the model: (1) Statistical evaluation using the ‘model skill score’ (Watterson, 1996)—a non-dimensional  
113 measure calculated using location-dependent comparisons between the model and an iodine ocean observation data  
114 compilation. (2) Graphical comparison of modeled and observed iodine across 3 illustrative iodine speciation gradients  
115 (depth profiles from multiple ocean basins, latitudinal transects of surface waters, and across transects of the Eastern  
116 Tropical North Pacific oxygen minimum zone (Moriyasu et al., 2020)). (3) Model applicability to ancient settings by  
117 comparing projections of ocean surface I:Ca with published I:Ca data from the Cretaceous (Zhou et al., 2015).

## 118 2. Model Description

### 119 2.1 The cGENIE Earth system modelling framework

120 cGENIE is a class of model known as an ‘Earth system model with intermediate complexity’ (EMIC)—a global  
121 climate-carbon cycle model that simplifies one or more (typically physical climatic) components of the Earth system.  
122 In the case of cGENIE, ocean circulation is solved for on a relatively low-resolution grid: an equal area 36×36 grid,  
123 which equates to 10° in longitude and latitude increments from 3° near the equator to 20° near the poles, and with 16  
124 non-equally spaced vertical levels. This is coupled to a 2D energy-moisture-balance-model (EMBM) and a 2D  
125 dynamic-thermodynamic sea-ice model. The physics are described in (Marsh et al., 2011; Edwards and Marsh, 2005).  
126 We use a parameter calibration of seasonal pre-industrial climate following Cao et al., (2009).



127 The primary factors controlling the oceanic iodine cycle—specifically, biological productivity,  
128 remineralization, and water column redox—are all represented in the model and described in Ridgwell et al., (2007).  
129 In that particular configuration, the rate of organic matter export from the ocean surface is calculated based on just a  
130 single nutrient (phosphate) control (together with light and sea-ice cover) and assumes a Redfield-ratio stoichiometry  
131 with carbon (Fig. 1). Organic matter is split into particulate (POM) (33% of total export) and dissolved form (DOM)  
132 (67%), with the former sinking down through the water column where it is progressively remineralized according to  
133 a prescribed fixed ‘decay’ curve, while the latter is physically transported by circulation and decays (is remineralized  
134 with a lifetime of 0.5 years). Here, we deviate from Ridgwell et al., (2007) (as well as the calibrated seasonal  
135 configuration of Cao et al., 2009) by adopting a calibrated temperature-dependence to both export production as well  
136 as the decay of POM in the water column (described in Crichton et al., 2021 and Boscolo-Galazzo et al., 2021).

137 Here, we use sulphate ( $\text{SO}_4^{2-}$ ) as an electron acceptor supporting the remineralization of organic matter (both  
138 POM and DOM) is governed by a  $\text{SO}_4^{2-}$  half-saturation limitation term as well as dissolved oxygen ( $\text{O}_2$ ) inhibition,  
139 while the rate of oxic respiration of organic matter is restricted by an  $[\text{O}_2]$  half-saturation limitation term (as described  
140 in Reinhard et al., 2020). This deviates from the framework described in Ridgwell et al., (2007). The difference is that  
141 here,  $\text{SO}_4^{2-}$  can be consumed even before dissolved oxygen can become fully depleted. Ambient temperature dictates  
142 the total fraction of POM that decays through both pathways per unit time and within each ocean depth layer (Crichton  
143 et al., 2021), with local  $[\text{O}_2]$  and  $[\text{SO}_4^{2-}]$  determining the fractional split between alternative pathways (Reinhard et al.,  
144 2020). For DOM, the decay constant determines the total fraction that decays per unit time. It should be noted that  
145 currently, there is no published nitrogen cycle in the cGENIE framework and hence we do not consider nitrate  
146 reduction as part of the redox cascade.

## 147 **2.2 Marine iodine cycling in cGENIE**

148 In the cGENIE model, iodine is present in three reservoirs:  $\text{IO}_3^-$  and  $\text{I}^-$  in the water column, and  $\text{I}^-$  incorporated in POM  
149 (and DOM). We then consider four processes that transfer iodine between these reservoirs: (1)  $\text{IO}_3^-$  reduction in the  
150 water column,  $\text{I}^-$  oxidation (also in the water column), photosynthetic  $\text{IO}_3^-$  uptake and intercellular reduction to  $\text{I}^-$ , and  
151  $\text{I}^-$  release to seawater during the remineralization of POM (and DOM) (Fig. 1). As dissolved tracers,  $\text{IO}_3^-$  and  $\text{I}^-$  are  
152 physically transported and mixed through ocean circulation (as is  $\text{I}^-$  incorporated into dissolved organic matter),  
153 whereas iodine in POM settles through the water column. This is effectively the same framework as used by Lu et al.,  
154 (2018). Here we re-assess this framework against an updated compilation of observed iodine speciation in the modern  
155 ocean and develop and test alternative representations of  $\text{IO}_3^-$  reduction (“threshold”, “inhibition” and  
156 “reminSO4lifetime”) and  $\text{I}^-$  re-oxidation (“lifetime”, “Fennel”, and “reminO2lifetime”).

157 In the numerical scheme of Lu et al., (2018), when  $[\text{O}_2]$  falls below a set concentration threshold,  $\text{IO}_3^-$  is  
158 immediately and quantitatively reduced to  $\text{I}^-$  (thereafter, we term this iodate reduction parameterization “threshold”).

159 The “inhibition” scheme links the  $\text{IO}_3^-$  reduction rate with the ambient  $\text{O}_2$  concentration. Following the  
160 formulation for the rate of  $\text{SO}_4^{2-}$  reduction in Reinhard et al., (2020), we apply an oxygen inhibition term governed by  
161 a half-saturation constant. In devising this scheme, we note that while  $\text{IO}_3^-$  reduction rates have been determined



162 experimentally, the quantitative relationship with  $[O_2]$  (or other parameters) is unknown. The  $IO_3^-$  reduction under  
 163 “inhibition” is mathematically described as:

$$164 \quad d[IO_3^-]/dt = [IO_3^-] \times k_{red} \times \frac{k_{O_2}}{k_{O_2} + [O_2]} \quad (1)$$

165 in which  $k_{red}$  is the maximum first-order reduction rate of  $IO_3^-$ , and  $k_{O_2}$  is the half-saturation constant of  $O_2$ .

166 Reduced sulfur (e.g. sulfides) is also suspected to play an important role in  $IO_3^-$  reduction in seawater,  
 167 especially in the sulfidic zones (Jia-zhong and Whitfield, 1986; Luther and Campbell, 1991; Wong and Brewer, 1977;  
 168 Truesdale et al., 2013). We therefore devise a scheme (“reminSO4lifetime”) that scales a nominal ‘lifetime’ for  $IO_3^-$   
 169 with the rate of  $SO_4^{2-}$  reduction in the model. This has the effect of increasing the rate of  $IO_3^-$  reduction (a shorter  
 170 lifetime) under conditions of higher sulphate reduction rates and hence lower ambient oxygen concentrations and/or  
 171 higher rates of organic matter degradation:

$$172 \quad d[IO_3^-]/dt = [IO_3^-] \times \frac{1}{\tau_{sul}} \times d[SO_4^{2-}]/dt \quad (2)$$

173 in which  $\tau_{sul}$  defines the rate constant parameter linking the  $IO_3^-$  and  $SO_4^{2-}$  reduction, while the  $d[SO_4]$  is amount of  
 174  $SO_4^{2-}$  reduced during each model timestep.

175 In Lu et al., (2018),  $I^-$  is oxidized to  $IO_3^-$  following first-order kinetics regardless of ambient  $O_2$  (scheme  
 176 “lifetime”). In this scheme,  $I^-$  oxidation follows the first-order reaction kinetics:

$$177 \quad d[I^-]/dt = [I^-] \times \frac{1}{\tau} \quad (3)$$

178 where  $\tau$  is the lifetime of  $I^-$  in seawater.

179 Given the potential link between  $I^-$  and nitrification, we devise an alternative “Fennel” scheme, in which  $I^-$   
 180 oxidation rates vary as a function of ambient  $O_2$ , increasing with ambient  $O_2$  concentrations towards some hypothetical  
 181 maximum value following Michaelis–Menten kinetics (Fennel et al., 2005). In Fennel et al., (2005), this  
 182 parameterization was originally devised for ammonia reoxidation. The form of this response is defined by the  
 183 maximum reaction rate and  $O_2$  half-saturation constant (Fennel et al., 2005):

$$184 \quad d[I^-]/dt = [I^-] \times k_{ox} \times \frac{[O_2]}{k_{fenn} + [O_2]} \quad (4)$$

185 in which  $k_{ox}$  defines the maximum rate constant of  $I^-$  oxidation, while  $k_{fenn}$  is the  $O_2$  half-saturation constant.

186 Finally, in “reminO2lifetime”, we associate  $I^-$  oxidation with  $O_2$  consumption during remineralization. The  
 187 logic behind this parameterization is the recent observation of  $I^-$  oxidation to  $IO_3^-$  catalyzed by bacteria, perhaps in  
 188 association with ammonia oxidation (Hughes et al., 2021). Although the nitrogen cycle is not currently included in  
 189 cGENIE, the  $NH_4^+$  oxidation can be scaled to OM remineralization (Martin et al., 2019) and hence to  $O_2$  consumption  
 190 during remineralization. Under “reminO2lifetime”, the lifetime of  $I^-$  oxidation is inversely linked to  $O_2$  consumption  
 191 so that faster remineralization—which in the ocean leads to more intensive  $NH_4^+$  oxidation—enhances  $I^-$  oxidation.  
 192 This  $I^-$  oxidation scheme follow this equation:

$$193 \quad d[I^-]/dt = [I^-] \times \frac{1}{\tau_{O_2}} \times d[O_2]/dt \quad (5)$$

194 where  $\tau_{O_2}$  is the rate constant parameter and  $d[O_2]$  is the  $O_2$  consumption during remineralization during a single  
 195 timestep in the model.

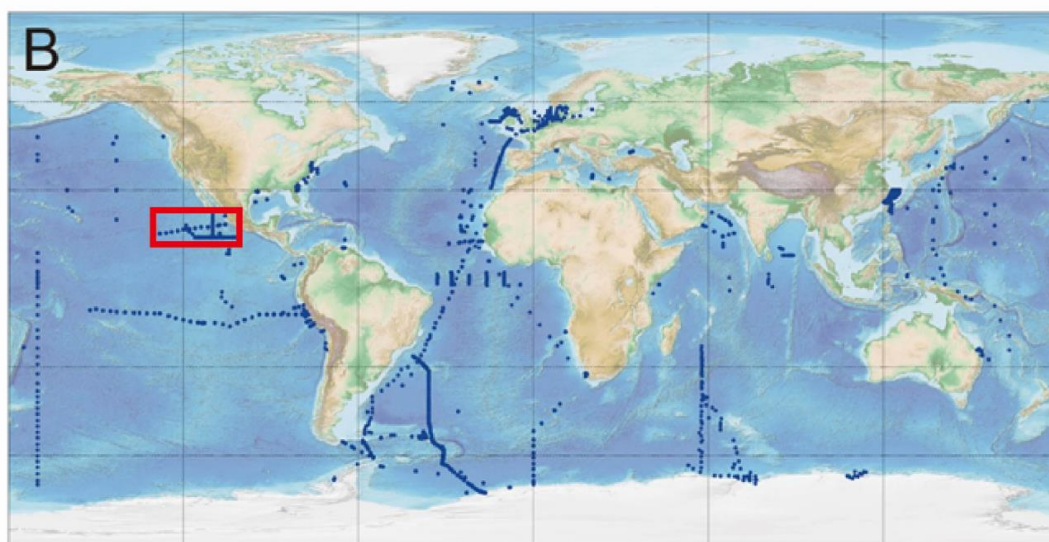
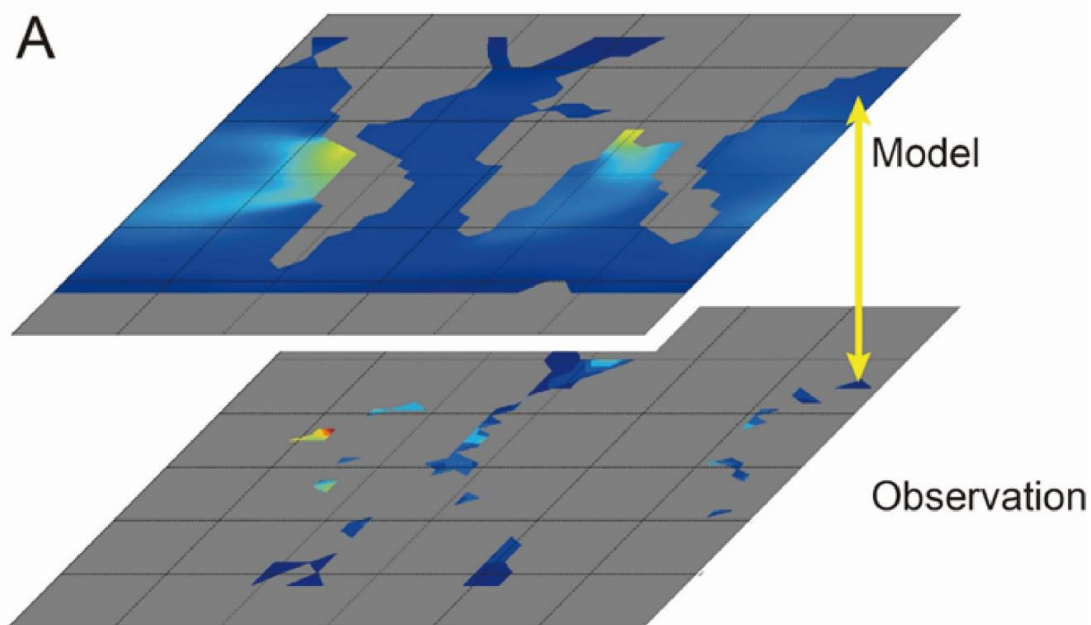


196                   The final process in the marine iodine cycle framework concerns the processing of iodine directly  
197 through the biological pump. In this,  $\text{IO}_3^-$  is taken up by phytoplankton and incorporated into OM during  
198 photosynthesis (Elderfield and Truesdale, 1980) before being released as  $\text{I}^-$  during remineralization and/or cell  
199 senescence (Wong et al., 2002; Hepach et al., 2020; Wong et al., 1985). cGENIE simulates these processes as a  
200 function of a ‘Redfield-ratio’ of iodine to carbon (I:C ratio) in OM. We note that while I:C is tunable, it is fixed  
201 throughout the ocean. We discuss the merits of an optimized and uniform I:C compared to variable I:C (e.g., Waddley  
202 et al., 2020) in more detail in the discussion.

### 203   **2.3   Model-data comparison**

204 We used the model skill measure (M) (Watterson, 1996) to assess the performance of the marine iodine cycle in  
205 cGENIE. A major advantage of the M-score is that it is calculated through location-dependent comparison (Fig. 2; Lu  
206 et al., 2018). Another advantage of the M score is that it captures overall improvement of model performance relative  
207 to model-minus-observation maps, since it is non-dimensional, and the higher M stands for better performance. For  
208 comparison with simulated distributions of iodine speciation, we compiled oceanic iodine observation data from the  
209 literature (Fig. 2B; Table S4). This dataset includes the compiled dataset of Chance et al., (2019) and Sherwen et al.,  
210 (2019), which was used to calibrate the Wadley et al., (2020) model, but includes more recent publications (referenced  
211 in Table S4) and is expanded to include the deep ocean and ODZ data. To avoid the influence of freshwater dilution  
212 and recycled iodine from the sedimentary flux, we applied a filter which only keeps the measurements with total iodine  
213 between 450nM and 550nM in the dataset. Note that the  $\text{I}^-$  measurements from the GP16 cruise in the ETSP are not  
214 included for the comparison because of potential method considerations (see Cutter et al., 2018 and Moriyasu et al.,  
215 2023). After these filtration methods, the data were re-gridded by taking the average values according to cGENIE  
216 grids. For each iodine speciation (hereby  $\text{IO}_3^-$  and  $\text{I}^-$ ), a M score is calculated through comparing re-gridded  
217 observations versus model results in each corresponding grid. The synthesized M score for iodine of each model  
218 experiment is calculated through averaging those for both  $\text{I}^-$  and  $\text{IO}_3^-$ .  
219





220

221 **Figure 2: A).** An example of location-dependent comparison between I- distributions in the cGENIE model  
222 **iodine data array and the regridded ocean observation. B).** The sampling locations of iodine observation data  
223 **used for model-data comparison. Some coastal stations included in the figure are filtered out in the model-data**  
224 **comparison. The ETNP transect associated with Fig.6 is labeled as red box.**

225

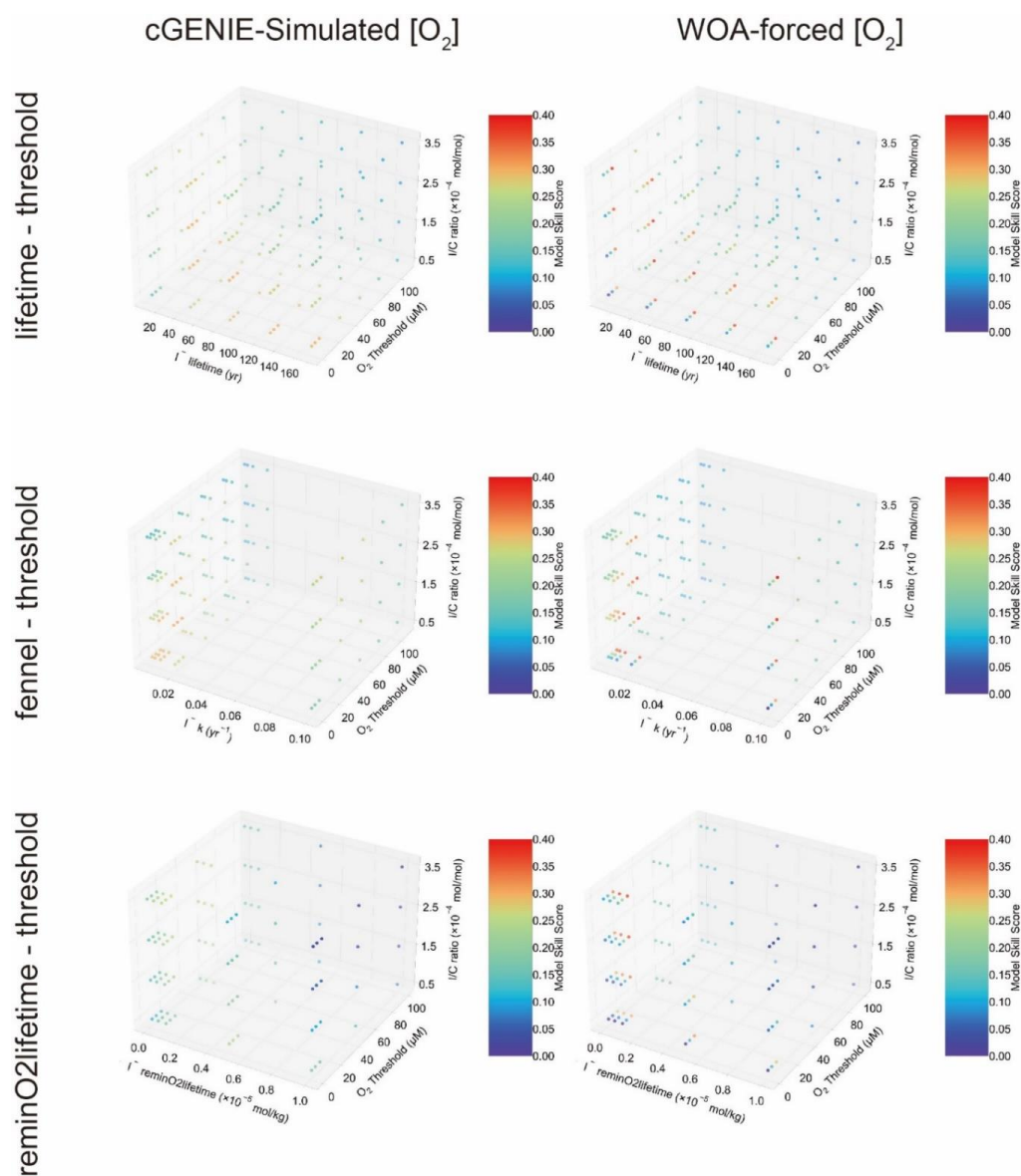




226 **2.4 Sensitivity analyses and model implementation**

227 Because the relative roles of  $\text{IO}_3^-$  reduction,  $\text{I}^-$  oxidation, and  $\text{IO}_3^-$  planktonic uptake in the water column are uncertain,  
228 we calibrate the parameters controlling these processes in cGENIE by creating an ensemble of different parameter  
229 value combinations arranged in a 2D regularly-spaced grid and then repeat the same 2D parameter ensemble for  
230 different assumptions of I:C (Fig. 3). The output of each ensemble member is then statistically compared to our  
231 observational database. We assume the associated parameterization when the model reaches the best M score of  
232 replicating modern ocean iodine distribution would also be applied to simulate iodine cycling in the past. Each  
233 ensemble member was run for a total of 2,000 years and each starts from the same initial state, which was an  
234 experiment run for 10,000 years to equilibrium using a random set of iodine parameters within the ranges in Table 1.  
235 Running the models for 2000 years minimizes the CPU time but was also found to be more than sufficient to allow  
236 iodine inventories to equilibrate to new steady states. To explore whether the model simulated dissolved oxygen  
237 distribution imparted any particular bias to the tuned iodine cycle, we repeated the model ensembles, continually  
238 restoring the 3D pattern of  $[\text{O}_2]$  in the model to that of the World Ocean Atlas 18 (WOA18) climatology (Garcia et  
239 al., 2018).

240



241

242 **Figure 3: The three-dimensional model skill score array of the experiment ensembles.**

243

244 We ran model ensembles to test five different combinations of iodine cycling parameterizations – “lifetime-threshold”,  
 245 “Fennel-threshold”, and “reminO2lifetime-threshold”, “lifetime-reminSO4lifetime”, “lifetime-inhibition” (Table S1).  
 246 While the results for all parameterization combinations are given in the supplement, we only focus on 3  
 247 parameterization-combinations here (Table 1) — “lifetime-threshold”, “Fennel-threshold”, and “reminO2lifetime-



248 threshold". (A detailed justification and discussion for selecting these parameterization-combinations is included in  
 249 the Discussion section.)

250

251 **Table 1. The cGENIE iodine redox options and the associated range of parameters of these options.**  
 252 **The detailed introduction of each parameter is described in section 2.2.2 and the plausibility of these parameter**  
 253 **ranges is discussed in 4.1.1. Note that the oxidation rate constant  $k$  in 'Fennel' is in unit of year<sup>-1</sup> in the model**  
 254 **configuration, which is the reciprocal of the 'lifetime'. A detailed table containing all considered**  
 255 **parameterization ranges can be found in Table S1.**

Parameter description	Iodine oxidation parameters			Iodine reduction parameters	I:C ratio ( $\times 10^{-4}$ mol/mol)	
	'lifetime' (years)	'reminO2lifetime' ( $\times 10^{-5}$ mol/kg)	'Fennel' (Inhibition constant/ $\mu\text{M O}_2$ )	'threshold' ( $\mu\text{M O}_2$ )		
Simulation 1	cGENIE O <sub>2</sub>	10-170	\	\	1-110	0.5-3.5
	WOA	10-170	\	\	1-110	0.5-3.5
Simulation 2	cGENIE O <sub>2</sub>	10-170 (1/k)	0.01-1	20	1-110	0.5-3.5
	WOA	10-170 (1/k)	0.01-1	20	1-110	0.5-3.5
Simulation 3	cGENIE O <sub>2</sub>	\	0.01-1	\	1-100	0.5-3.5
	WOA	\	0.01-1	\	1-100	0.5-3.5

256



257 **3. Results**

258 In this section, we start by summarizing the overall statistical outcome of the tuning, then present a series of spatial  
259 analysis comparisons for each of the highest M-score ensemble members. The spatial analyses progressively reduce  
260 in scale, moving from global surface distributions, to global and basin-specific water column profiles, and finally to  
261 spatial comparisons for a specific ODZ region.

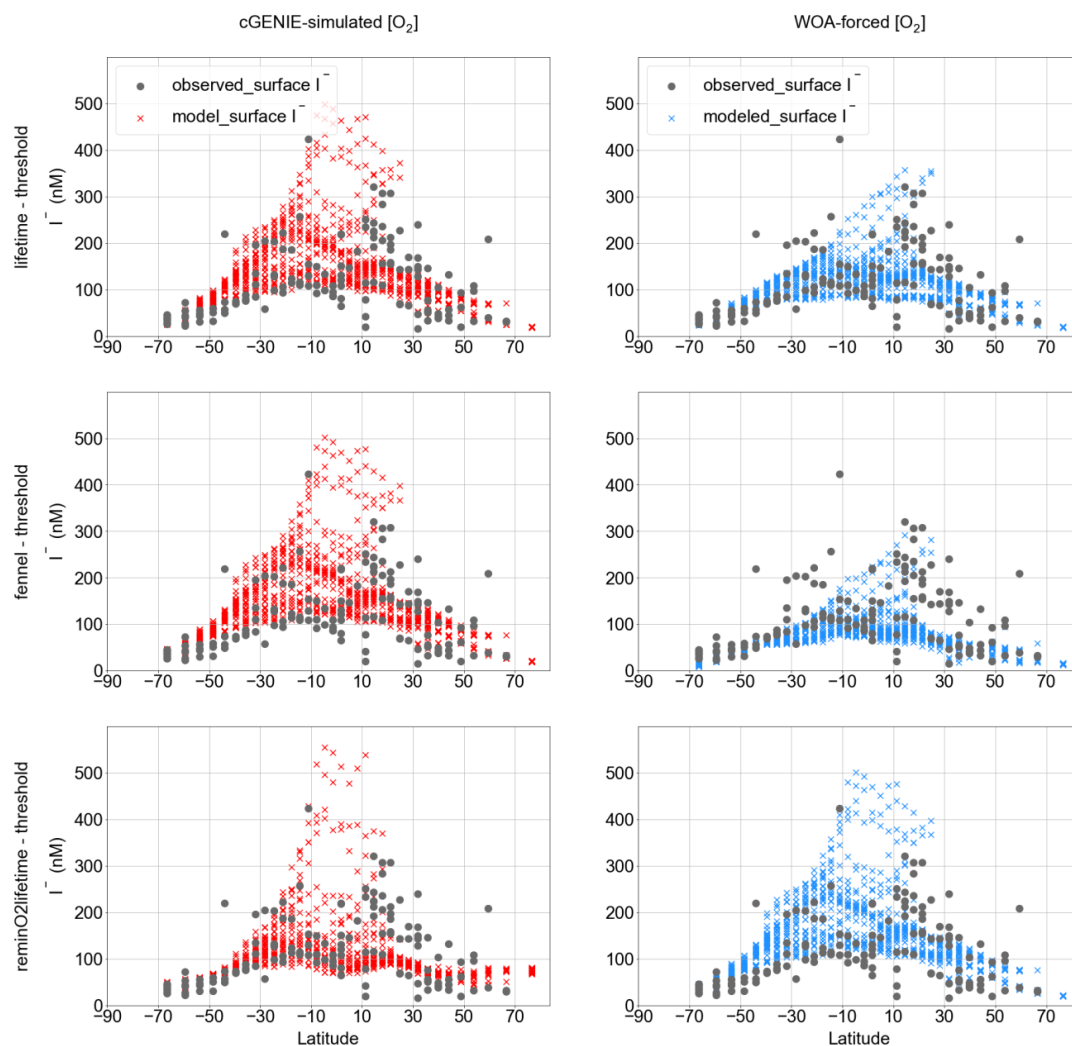
262 **3.1. Model skill score**

263 The M-score values achieved across the complete ensemble for each of the 3 main parameterization-combinations are  
264 illustrated in Fig. 3. The sensitivity test shows the M scores are sensitive to all three of the main parameters for the  
265 ensembles in Fig. 3. Higher model skill scores are usually reached when “threshold” is tuned to 10  $\mu\text{M}$   $[\text{O}_2]$  for all the  
266 ensembles, including both model-simulated  $[\text{O}_2]$  and WOA-forced  $[\text{O}_2]$ . For the ensembles, “lifetime-threshold” and  
267 “Fennel-threshold”, the highest M scores are similar—0.305 and 0.308, respectively (Table 2). Both these ensembles  
268 have the highest performance when “threshold”, “lifetime”, and I:C ratio are tuned to 10  $\mu\text{M}$   $[\text{O}_2]$ , 50 years, and  $1.5$   
269  $\times 10^{-4}$  mol/mol, respectively, which is generally consistent with observations (Lu et al., 2016, 2020b; Tsunogai, 1971;  
270 Elderfield and Truesdale, 1980) (discussed in more detail later). The model performance of “reminO2lifetime-  
271 threshold” is less good than the other two combinations, with the best M score of 0.266 when “threshold”,  
272 “reminO2lifetime”, and I:C ratio are tuned to 10  $\mu\text{M}$   $\text{O}_2$ ,  $1 \times 10^{-6}$  mol/kg, and  $3.5 \times 10^{-4}$  mol/mol, respectively (Table  
273 2, Fig. 3). We note that for each parameterization-combination, the highest possible M score achievable by tuning  
274 improves when  $[\text{O}_2]$  is forced to that of the World Ocean Atlas 18 (WOA18) climatology (Garcia et al., 2018).

275 **3.2. Meridional surface I<sup>-</sup> distribution**

276 Figure 4 shows a comparison between the observed latitudinal distribution of  $[\text{I}^-]$  at the surface and as simulated by  
277 the model for each parameterization-combination (for the respective best M-score ensemble member). Note that the  
278 observations (Section 2.3) are binned to the corresponding model grid cells and as such, reflect averages over the  
279 upper-most 80 m of the water column. This represents a reduction from 1338 to 141 surface ocean data points. We  
280 find that the surface ocean  $[\text{I}^-]$  in the model shows a trend of increasing values towards low latitudes, broadly consistent  
281 with observations (Chance et al., 2014) (Fig. 4). The “lifetime-threshold” and “Fennel-threshold” show similar  
282 latitudinal trends, but both overestimate the surface I<sup>-</sup> in the mid-low latitudes in the southern hemisphere. The  
283 “reminO2lifetime-threshold” ensemble produces better estimation of meridional surface  $[\text{I}^-]$  trend, although  
284 overestimates  $[\text{I}^-]$  in the tropical surface ocean compared to the other two ensembles (Fig. 4).

285



286

287 **Figure 4: Modeled latitudinal surface iodide distribution compared with observation with the cGENIE**  
 288 **simulated [O<sub>2</sub>] and the [O<sub>2</sub>] restoring forcing. The elevated [I<sup>-</sup>] observed and modeled in low latitudes is the**  
 289 **result of phytoplankton reduction in the surface ocean. Note that the I<sup>-</sup> distribution simulated by “lifetime-**  
 290 **threshold” and “fennel-threshold” are close but not identical.**

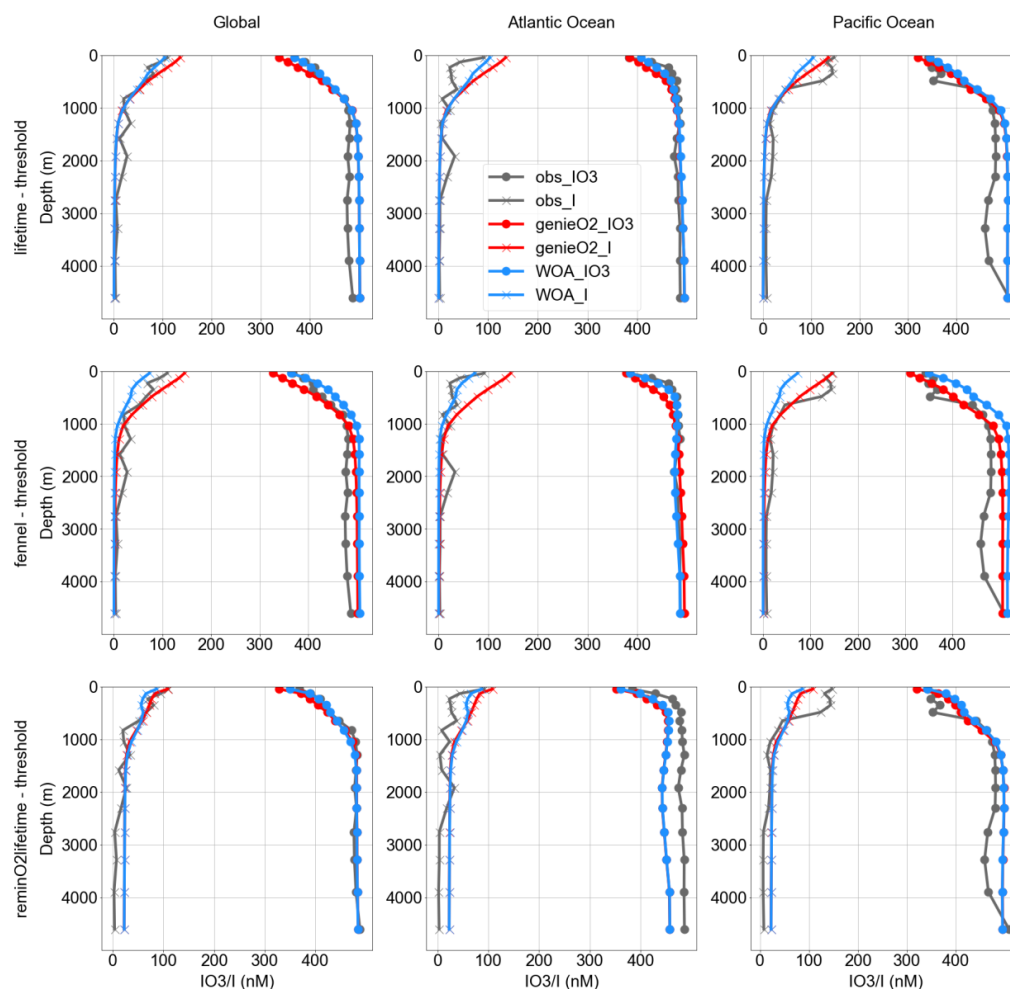
291

### 292 3.3. Global and basin-specific iodine depth distributions

293 Comparisons between the observed distributions of I<sup>-</sup> and IO<sub>3</sub><sup>-</sup> seawater concentrations among the global ocean and  
 294 the Atlantic and Pacific Oceans are presented in Fig. 5. Again, we re-gridded the iodine observations (see: Section 2.4)  
 295 and selected sub-sets of the data that lay in either Atlantic or Pacific basins, contrasting with the corresponding model  
 296 values at those locations. We find only relatively minor differences between the best M-score ensemble member of



297 each of all three parameterization-combinations, and all show increased  $[IO_3^-]$  and decreased  $[I^-]$  with increased depth  
 298 below the photic zone in the Atlantic and Pacific basins, as well as globally (Fig. 5). The modeled depth profile broadly  
 299 matches with observation in the Atlantic and deep Pacific Ocean, except the underestimated subsurface peak of  $[I^-]$   
 300 observed in the Pacific and overestimated  $[IO_3^-]$  in the deep Pacific (Fig. 5). This mismatch of subsurface  $I^-$  peak is  
 301 probably the result of sampling bias, with most of the Pacific iodine observations from ODZs in the Eastern Tropical  
 302 North Pacific (ETNP) and the Eastern Tropical South Pacific (ETSP). For example, in model depth profiles masked  
 303 to only include grid points with corresponding observations, the modelled Pacific depth profiles show a clear mid-  
 304 depth ODZ feature (Fig. S8).  
 305



306

307 **Figure 5: Modeled averaged iodine (including iodate and iodide) depth profile among global ocean, the Pacific,**  
 308 **the Atlantic compared with observation. The surface  $I^-$  enrichment among the ocean basins is caused by**  
 309 **phytoplankton reduction. The subsurface (~500m)  $I^-$  enrichment is the result of sampling bias that most of the**  
 310 **observations are from the ETNP and ETSP ODZs.**



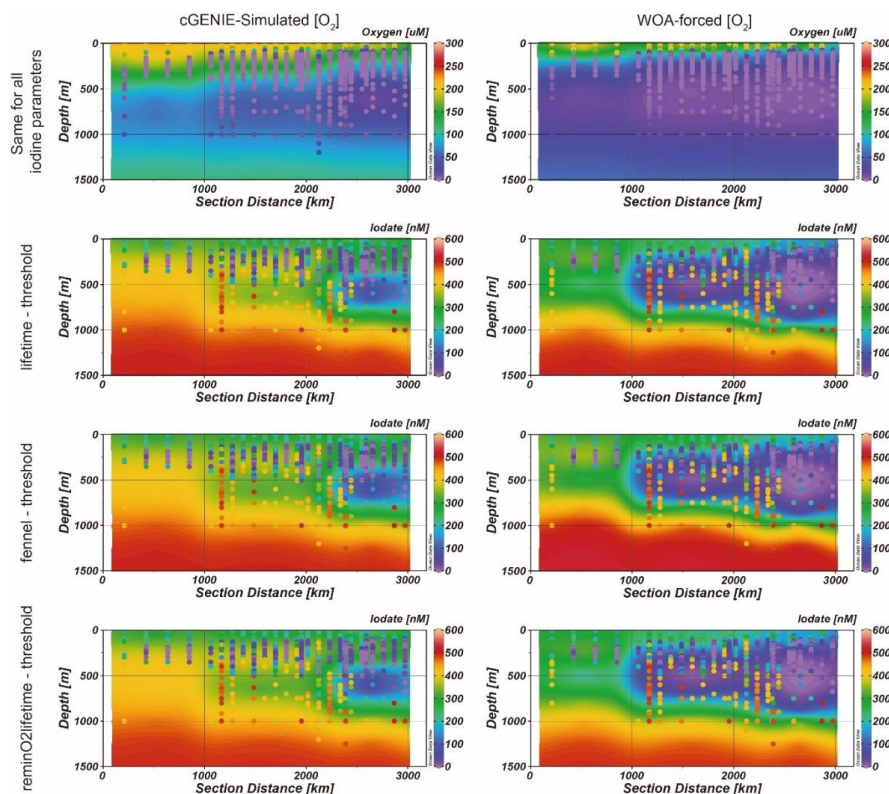


311

312 **3.4. Iodine distribution within ODZs**

313 To assess the model ability to simulate iodine cycling in marine low oxygen environments, we compared distributions  
 314 of oxygen and iodine species in the ETNP (Fig. 6). The O<sub>2</sub> transects amongst all model simulations are the same  
 315 because we only changed the parameterizations of the iodine cycle between ensembles and ensemble members (i.e.,  
 316 they all simulate the same biological pump in the ocean). Notably, compared to [O<sub>2</sub>] measured in the ETNP transect,  
 317 the model underestimates the extent of the ODZ. Severe deoxygenation below 50 μM [O<sub>2</sub>] was observed in relatively  
 318 shallow depths between 100-200m in the ETNP, and this ODZ extends for more than 3000 km towards off-shore from  
 319 Mexican coast (Fig. 6). Although cGENIE simulates the O<sub>2</sub>-deficient pattern in the ETNP, the extent of the ODZ is  
 320 underestimated. The simulated oxycline is ~200m deeper than the observation and the [O<sub>2</sub>] variation is gradual. The  
 321 ODZ below 20 μM [O<sub>2</sub>] in the model is limited to a small spatial extent within 1000km offshore, which is much smaller  
 322 than that in the observation (Fig. 6).

323



324

325 **Figure 6: Modeled (contour) and observed (colored dots) west-to-east transect of IO<sub>3</sub><sup>-</sup> and O<sub>2</sub> in the ETNP. Note**  
 326 **that the WOA-forced [O<sub>2</sub>] models simulate a larger extent of IO<sub>3</sub><sup>-</sup> anomaly, which better matches the**  
 327 **observation. The left-hand panel contours are model results based on cGENIE-simulated [O<sub>2</sub>] while contours**  
 328 **on the right are model results from WOA-forced [O<sub>2</sub>].**



329

330 All the three chosen best-performance-experiments show similar iodine anomalies ( $\text{IO}_3^-$  depletion) in the  
 331 ETNP, fitting the general feature of the observation. Other parameterizations did not replicate the ODZ (Fig. S4).  
 332 However, even under the “best-fitting” parameters, compare to the observations, the ODZ feature in the model is  
 333 underestimated both in intensity and in areal extent compared to the observations (Fig. 6). The observed  $\text{IO}_3^-$  depletion  
 334 zone ( $[\text{IO}_3^-] < 100\text{nM}$ ) occurs in shallower depths between 100-500m, matching the shallow ODZ and spans ~2000km  
 335 offshore; however, the modeled  $\text{IO}_3^-$  depletion zones in the ETNP are located in 400-700m, and only extends within  
 336 1000km from the shore.

337 We also ran model ensembles forcing cGENIE to restore the modern ocean  $[\text{O}_2]$  annual average climatology  
 338 to that of the WOA18 (Garcia et al., 2018) (Fig. 6). Now the subsurface  $\text{IO}_3^-$  depletion zone in the ETNP ODZ in all  
 339 three ensembles extends ~2000km offshore and spans across 100-1000m in depth (Fig. 6). The shallow and extended  
 340 ODZ iodine distribution in the ETNP better matches the observation compared to non- $\text{O}_2$  restoration simulations.

341

342 **Table 2. The performance of the cGENIE iodine simulations and associated parameterization when the**  
 343 **model reaches the best global M score. Note that the oxidation rate constant  $k$  in ‘Fennel’ is in unit of  $\text{year}^{-1}$  in**  
 344 **the model configuration, which is also the reciprocal of the ‘lifetime’. The full model performance is**  
 345 **summarized in Table S2. Note that the lifetime in ‘Fennel’ is parameterized as  $k (\text{year}^{-1}) = 1/\text{lifetime}$ .**

Parameter description	Iodine oxidation parameters			Iodine reduction parameters	I:C ratio ( $\times 10^{-4}$ mol/mol)	Model skill score	
	'lifetime' (years)	'reminO2lifetime' ( $\times 10^{-5}$ mol/kg)	'Fennel' (Inhibition constant/ $\mu\text{M O}_2$ )	'threshold' ( $\mu\text{M O}_2$ )			
Simulation 1	cGENIE $\text{O}_2$	50	\	\	10	1.5	0.305
	WOA	50	\	\	10	1.5	0.385
Simulation 2	cGENIE $\text{O}_2$	50 (1/k)	\	20	10	1.5	0.308
	WOA	10 (1/k)	\	20	10	3.5	0.385
Simulation 3	cGENIE $\text{O}_2$	\	0.1	\	10	3.5	0.266
	WOA	\	0.1	\	10	3.5	0.365

346



## 347 4. Discussion

348 In summary: we ran ensembles for five combinations of iodine cycling parameters (summarized in Table S2) in the  
349 cGENIE Earth system model (both with internally calculated and WOA-imposed  $[O_2]$  distribution) and presented  
350 the results for 3 of them that showed the best performance. We analyzed the performance of the ensembles via: (1)  
351 M score for the model-data match of both  $[I^-]$  and  $[IO_3^-]$  across the entire ocean, (2) qualitative model-observation  
352 comparison of latitudinal surface ocean distributions of  $[I^-]$ , (3) averaged depth profiles in global and individual  
353 ocean basins for both  $[I^-]$  and  $[IO_3^-]$ , (4) iodine transects across the Eastern Tropical North Pacific  
354 (ETNP) ODZ, and (5) M score for model and I:Ca observations for pre-OAE2.

### 355 4.1. Overall model skill score comparison

356 Two broad observations emerge from the M score comparison. First, the 1<sup>st</sup>-order kinetic iodine oxidation associated  
357 ensembles (“lifetime-threshold” and “Fennel-threshold”) have the highest M scores (Table 2), under both cGENIE-  
358 simulated  $[O_2]$  and WOA-forced  $[O_2]$ . This is consistent with previous observations of 1<sup>st</sup>-order kinetics for  
359  $I^-$  oxidation (Tsunogai, 1971). Second, the simulations with WOA-forced  $[O_2]$  produce significantly higher M  
360 scores than that of the cGENIE-simulated  $[O_2]$  field (at least ~0.8 of improvement; Table 2). Despite a 1<sup>st</sup>-order non-  
361  $O_2$  dependent oxidation mechanism providing the highest M scores, the WOA vs internally model-generated  
362 dissolved oxygen distributions comparison highlights the  $O_2$  and related redox dependency of the iodine cycle from  
363 the perspective of  $IO_3^-$  reduction. Each of these factors are discussed in the following Section 4.1.1.

#### 365 4.1.1. Parameter value plausibility

366 A credible representation of the marine iodine cycle requires not only that observations can be replicated, but that  
367 replication occurs when parameter values fall within real-world ranges. In this section, we discuss the validity of our  
368 best-fit (maximized M-score) parameter values. For the iodine cycle, these parameters include  $O_2$  threshold, I:C ratio,  
369 and  $I^-$  oxidation rate.

370 Our model M score is highest with an  $[O_2]$  reduction threshold of  $10\mu M$  (Fig. 3 and Table 2). Although it is  
371 generally well accepted that  $IO_3^-$  is reduced in low oxygen settings (Luther, 1991; Rue et al., 1997; Wong et al., 1985;  
372 Wong and Brewer, 1977; Farrenkopf and Luther, 2002), the degree of  $O_2$  depletion that triggers  $IO_3^-$  reduction is still  
373 unclear. A relative high threshold for triggering  $IO_3^-$  reduction is proposed based on comparison between benthic  
374 foraminiferal I:Ca and ambient  $[O_2]$  (20-70  $\mu M O_2$ ; Lu et al., 2016, 2020a). These  $[O_2]$  thresholds are similar to that  
375 determined in a previous cGENIE-based iodine cycle study (30  $\mu M$ ) (Lu et al., 2018), but it is difficult to directly  
376 compare this to our results because of differences in the model representation of the ocean biological pump, the iodine  
377 observational data-set, and model-data comparison methods utilized.

378 Many of the studies suggesting a relatively high  $[O_2]$  threshold is based on evaluations of  $[IO_3^-]$ - $[O_2]$  within  
379 the upper chemocline of ODZs; however, evaluation of  $[O_2]$ - $[IO_3^-]$  from ODZs throughout the entire water column  
380 suggest the potential for  $IO_3^-$  persistence within the low oxygen cores of ODZs. Specifically,  $IO_3^-$  accumulation is  
381 observed within the ETNP and ETSP at depths where  $[O_2]$  is close to or below the detection limit of the sensors which  
382 is reported near 1  $\mu M$  (Hardisty et al., 2021). In addition, it is worth noting that the kinetics of  $IO_3^-$  reduction is  
383 heterogeneous both within and between ODZs. For example, a transect evaluating  $IO_3^-$  reduction rates in the ETNP



384 observed rapid rates in the upper oxycline, where  $[O_2]$  was near  $\sim 12 \mu M$ , but the potential for sluggish rates in the  
385 ODZ cores, where  $[O_2]$  was below detection. In an early study of the Arabian Sea,  $IO_3^-$  was reduced rapidly within  
386 the ODZ core. Together, these suggest  $IO_3^-$  reduction may be controlled by factors beyond  $O_2$  (Hardisty et al., 2021;  
387 Farrenkopf and Luther, 2002). For example,  $IO_3^-$  is likely formed in high  $[O_2]$ , non-ODZ water masses but can be  
388 sustained upon transport or mixing within oligotrophic, offshore ODZ regions where organic supplies are more limited  
389 (Hardisty et al., 2021). A comparison to the N cycle would also indicate a low  $[O_2]$  threshold—for example,  
390 denitrification has a sub- $\mu M$   $[O_2]$  threshold and has a similar redox potential with  $IO_3^-$  reduction (Dalsgaard et al.,  
391 2014; Thamdrup et al., 2012). A sub- $\mu M$   $[O_2]$  threshold for  $IO_3^-$  reduction could explain the  $[IO_3^-]$  variations observed  
392 in ODZ cores with  $[O_2]$  below the  $\mu M$  detection limits of sensors; however, iodine speciation has yet to be analyzed  
393 alongside  $[O_2]$  measurements via sensors with sub- $\mu M$  detection limits, such as STOX sensors. Regardless, our 10  
394  $\mu M$   $[O_2]$  threshold based on maximizing the M score reflects a global average value and clearly falls within the ranges  
395 of oceanographic observations.

396 For both our study and that of Lu et al., (2018), an I lifetime of 50 years maximizes model performance.  
397 However, Lu et al., (2018) chose to implement a slightly lower value of 40 years for their paleo-application because  
398 it reflected the slowest rate observed in the literature at that time (Tsunogai, 1971). Notably, though  $IO_3^-$  is the most  
399 abundant marine iodine species, its production from I<sup>-</sup> has never been observed under normal marine conditions. This  
400 has acted as a major hinderance on providing direct constraints. That said, our cGENIE estimate is consistent with a  
401 multitude of other constraints that indicate that I<sup>-</sup> oxidation to  $IO_3^-$  undergoes extremely slow kinetics. The I<sup>-</sup> oxidation  
402 rates calculated through indirect methods including mass balance and seasonal iodine speciation changes (Tsunogai,  
403 1971; Campos et al., 1996; Truesdale et al., 2001; He et al., 2013; Edwards and Truesdale, 1997; Žic et al., 2013;  
404 Moriyasu et al., 2023) or through radiogenic tracer spiked incubations (Hardisty et al., 2020; Schnur et al., 2024;  
405 Ștreangă et al., 2024) have a wide range of variation from 1.5nM/yr to 670nM/yr. The lifetime in cGENIE is 50 years,  
406 which can be approximately converted to the zeroth order rate of  $< 9$  nM/yr, falling in the lower end of the previous  
407 studies.

408 Our best-fit I:C ratio is  $1.5 \times 10^{-4}$ , and this value is in agreement with plankton measurements and mass-  
409 balance calculations (Chance et al., 2010; Elderfield and Truesdale, 1980). In the photic zone,  $IO_3^-$  is taken up by  
410 phytoplankton and incorporated into their cellular structures followed by subsequent conversion into I<sup>-</sup> (Hepach et al.,  
411 2020). Due to this, it is assumed that  $IO_3^-$  removal in the surface layer of the ocean is a function of organic carbon  
412 fixation during primary productivity according to Redfield-like ratios (Campos et al., 1996; Chance et al., 2010). Of  
413 the parameters incorporated into the model, in theory, I:C should probably be the best constrained. However, published  
414 I:C ratios based on field and laboratory measurements vary over several orders of magnitude ( $10^{-5}$  to  $10^{-3}$ ) (Elderfield  
415 and Truesdale, 1980; Campos et al., 1996; Hepach et al., 2020; Chance et al., 2010). To limit the number of model  
416 simulations and size of the ensembles, we only varied I:C between  $5 \times 10^{-5}$  and  $3.5 \times 10^{-4}$ , increasing by  $1.0 \times 10^{-4}$ , which  
417 covers the range indicated by previous studies (Elderfield and Truesdale, 1980).

418 It is unlikely that the I:C value is constant across the global ocean due to differences in phytoplankton compositions  
419 and other factors. In cGENIE, most of the elevated surface  $[I^-]$  over 200nM is present in the ETSP and the northern  
420 Indian Ocean, representing the effect of high primary productivity and transformation of  $IO_3^-$  to I<sup>-</sup> via the rapid



421 recycling DOM ‘loss term’ in the representation of biological export (Fig. S6). The mismatch between the model and  
422 the observation probably hints that the I:C ratio is not constant in the ocean, as which is also hypothesized by Wadley  
423 et al., (2020), although in the absence of an explicit representation of primary productivity in the model and lack of a  
424 spatially variable f-ratio (Laws et al., 2000)(implicitly, the f-ratio is 0.33 everywhere in cGENIE). In testing a fixed,  
425 spatially uniform I:C, Wadley et al. (2020) underestimated surface [I<sup>-</sup>] in low latitudes and overestimated  
426 concentrations in mid-latitudes. Based on their model-observation comparison, they hypothesized that the I:C ratio  
427 decreases systematically with sea surface temperature (SST) (Wadley et al., 2020). Until more constraints are  
428 developed on spatial variability and associated driving factors for I:C, a generalized approach of a globally uniform  
429 I:C remains the most parsimonious assumption, especially considering cGENIE’s intended extrapolation to ancient  
430 settings.

#### 431 **4.1.2. Comparing alternative iodide oxidation parameterizations in cGENIE**

432 Due to similarity in redox potentials, the iodine cycling in the ocean has been hypothesized to be linked to the cycling  
433 of nitrogen (Rue et al., 1997). Nitrification promoting I<sup>-</sup> oxidation to IO<sub>3</sub><sup>-</sup> has been hypothesized in field studies  
434 (Truesdale et al., 2001; Žic et al., 2013), and more recently has been linked via observation of I<sup>-</sup> oxidation to IO<sub>3</sub><sup>-</sup> by  
435 ammonia oxidizing bacteria in laboratory environments (Hughes et al., 2021). We further note that Wadley et al.,  
436 (2020) explicitly link I<sup>-</sup> oxidation to NH<sub>4</sub><sup>+</sup> oxidation in their surface ocean iodine cycle model.

437 As an alternative to the first-order lifetime oxidation parameterization used here and in Lu et al., (2018) and  
438 in the current absence of a full nitrogen cycle (and hence explicit NH<sub>4</sub><sup>+</sup> oxidation) in cGENIE, we also applied a  
439 strategy (“reminO2lifetime”) which links I<sup>-</sup> oxidation to organic carbon remineralization and the consumption rate of  
440 dissolved oxygen. The reasoning behind this is that the O<sub>2</sub> consumption rate in the model implicitly reflects bacterial  
441 oxidizing activity in the water column and hence the potential for I<sup>-</sup> to be oxidized to IO<sub>3</sub><sup>-</sup>.

442 We find that the overall model performance involved with the “reminO2lifetime” is lower than other  
443 experiments where I<sup>-</sup> oxidation is ubiquitously oxidized according to a parametrized lifetime, or “lifetime-threshold”  
444 (maximum M score 0.266 vs. 0.305/0.308 under cGENIE simulated [O<sub>2</sub>]) (Fig. 3 and Table 2). However, despite  
445 slightly lower M scores, the “reminO2lifetime” generally replicates the latitudinal surface [I<sup>-</sup>] trend, the depth profiles  
446 in the ocean basins, and the ODZ transect (Figs. 4-6).

447 Under the default “lifetime” scheme, I<sup>-</sup> will oxidize in the whole ocean regardless of the concentration (or  
448 even presence/absence) of ambient O<sub>2</sub>. This scenario might hence not perform well in replicating the ocean iodine  
449 cycling at intervals during the Phanerozoic when ODZs were highly expanded, or particularly during the Precambrian  
450 when the majority of the ocean was ferruginous or euxinic and highly depleted in O<sub>2</sub> (for example, summarized by  
451 Lyons et al., 2014). Ideally, for application to paleoceanographic studies, an [O<sub>2</sub>]-related I<sup>-</sup> oxidation alternate scheme  
452 is required. Although thermodynamics theory suggests O<sub>2</sub> does not directly drive I<sup>-</sup> oxidation (Luther et al., 1995),  
453 field studies in ODZs indeed observed low [O<sub>2</sub>] inhibits this process (Farrenkopf and Luther, 2002; Moriyasu et al.,  
454 2020). We hence developed and tested variable I<sup>-</sup> oxidation kinetics, with the ambient dissolved O<sub>2</sub> providing an  
455 inhibition of the rate of oxidation based on the enzymatic nitrification scheme of Fennel et al., (2005).



456 Since most of the ocean is fully oxygenated today, the difference of M scores between “lifetime” and “Fennel”  
457 oxidation models are minor (0.305 vs. 0.308, Table 2). The parameters associated with the highest M score between  
458 two oxidation options are also very close to each other, except “Fennel” oxidation together with the model WOA-  
459 forcing, has higher I:C ratio ( $3.5 \times 10^{-4}$ ) and faster saturated I<sup>-</sup> oxidation kinetics (0.1 yr<sup>-1</sup> vs. 0.02 yr<sup>-1</sup> in other  
460 ensembles). The parameter differences between the “Fennel”-WOA ensemble and other models make sense because  
461 the faster oxidation rate compensates the increased I<sup>-</sup> production through the higher biotic uptake rate. The pre-OAE2  
462 simulations are particularly illustrative of this tradeoff and are discussed in more detail in section 4.3.

463 In summary, all the three parameter combinations produce high and comparable M scores and similar  
464 parameters (oxidation, reduction, and I:C) associated with these M scores (Table 2). Although direct field-based  
465 evidence to evaluate the controlling parameters of “reminO2lifetime” is absent, the parameters controlling the other  
466 model scheme are consistent with previous studies.

#### 467 **4.2. Beyond the M-score: model-data comparison across iodine gradients**

468 As applied here, the M score provides a quantitative measure that describes the overall model global performance and  
469 allows us to directly compare the implications of parameter value and parameterization choices. However, the M score  
470 overlooks regional gradients that may be important for both paleo- and modern oceanographic research. Indeed,  
471 amongst all the various ensembles we ran as part of this study (Table S1), only “lifetime-threshold”, “lifetime-Fennel”,  
472 and “reminO2lifetime-threshold” performed well in replicating the modern oceanic iodine gradients (Figs. S2-S4) and  
473 informed our decision to focus on these 3 parameterization-combinations here. We now discuss this in more detail  
474 below.

##### 475 **4.2.1. Meridional surface [I<sup>-</sup>] gradient**

476 All the parameterization-combinations summarized in Table 2, as well as the observations, show enrichment of I<sup>-</sup> in  
477 the surface ocean at low latitudes (Fig. 4). The pathway of transforming IO<sub>3</sub><sup>-</sup> into I<sup>-</sup> in these oxidized waters is through  
478 primary productivity in the photic zone, which is temperature dependent (Chance et al., 2014). A recent north-south  
479 transect showed the highest surface I<sup>-</sup> enrichment in the oligotrophic, permanently stratified tropical stations (Moriyasu  
480 et al., 2023). Therefore, the IO<sub>3</sub><sup>-</sup> flux from deep waters through seasonal mixing may be an important balance to *in-*  
481 *situ* IO<sub>3</sub><sup>-</sup> reduction rate by primary producers in the high latitudes (Chance et al., 2014; Moriyasu et al., 2023). The  
482 cGENIE model generates the general pattern of latitudinal surface I<sup>-</sup> distribution pattern; however, overestimation  
483 especially in low latitudes may exist, especially in the tropical surface where [I<sup>-</sup>] are close to 500nM among all the  
484 cGENIE-O<sub>2</sub> models (Fig. 4).

485 The cGENIE (internally generated oxygen distributions) vs WOA (imposed distributions) O<sub>2</sub> comparison  
486 provides evidence that I<sup>-</sup> generated in low [O<sub>2</sub>] settings may broadly enhance [I<sup>-</sup>] in oxygenated photic waters, with  
487 lower and closer-to-observations [I<sup>-</sup>] values in the WOA tunings (Fig. 4). This includes “lifetime-threshold”, where  
488 O<sub>2</sub> only impacts the reductive portion of the iodine cycle, but also the “Fennel” and “reminO2lifetime” where rates of  
489 I<sup>-</sup> oxidation is also [O<sub>2</sub>] dependent. More specifically, most of the elevated (over 200nM) surface [I<sup>-</sup>] in cGENIE,  
490 occurs in the ETSP and the northern Indian Ocean and corresponds to locations of high primary productivity (Fig. S6).





491 Since the surface ocean  $[O_2]$  in the model is never below  $200\mu M$ ,  $IO_3^-$  reduction at the ocean surface is unlikely.  
492 Instead, *ex situ* transport from proximal regions of subsurface anoxia is the most probable source of elevated  $I^-$ . Indeed,  
493 the most prominent regions of  $I^-$  enrichment in the model occur near the Peruvian coast and in the Arabian Sea, where  
494 ODZs lie below the surface (Fig. S6). More detailed data-model comparison among these two areas is limited because  
495 the observation data are few (e.g., Farrenkopf and Luther, 2002 and Rapp et al., 2020). In contrast, the meridional  
496 trend of  $I^-$  in the surface Atlantic Ocean, where ODZs are less developed, exhibits better agreement with both the  
497 observation and the Wadley et al., (2020) model (Fig. S6). The overestimation of tropical ocean surface  $[I^-]$  by cGENIE  
498 is hence likely to be associated with deficiencies in the simulation of ODZ oxygenation.

499 Importantly, modeled overestimations in surface ocean  $[I^-]$  may be difficult to confirm given current  
500 observational data densities. Specifically, a comparison of observational data to model-latitude trends masked to  
501 only include grid points with corresponding observations show the same broad trend of increasing  $[I^-]$  in the low  
502 latitude but with fewer so called “overestimations” (Fig. S7). More observations in surface ocean  $[I^-]$  from low  
503 latitudes is required to better assess the validity of elevated modelled surface ocean  $[I^-]$  in some regions.

#### 504 4.2.2. Global and basin-specific iodine depth profiles

505 All the models, both cGENIE- $[O_2]$  and WOA-forced, generate a decrease in  $[I^-]$  and increase in  $[IO_3^-]$  from the  
506 euphotic zone down to the deep abyssal zone across ocean basins, matching the primary-production-driven pattern  
507 (Fig. 5). As discussed in the previous section, this surface maxima of  $[I^-]$  in the oxygenated water column is the result  
508 of biologically mediated reduction or release during cell senescence of phytoplankton. Below the photic zone,  $[I^-]$  is  
509 close to zero and  $IO_3^-$  becomes the dominant species. The deep ocean is mostly oxygenated and has longer water  
510 residence times (several millennia, Matsumoto, (2007)) compared to the  $I^-$  lifetime ( $<40$  years, Tsunogai, (1971)), thus  
511 facilitating  $I^-$  oxidation in the absence of  $IO_3^-$  reduction in ODZs.

512 We note that there are multiple general discrepancies between observations and data as well as differences  
513 between WOA and cGENIE- $[O_2]$ . In general, all models reproduce the global average better, relative to the basin-  
514 specific profiles. We suggest that the global averaged profiles are a better test of the cGENIE simulations because of  
515 sampling biases associated with individual basins. For example, the discrepancy between the model and the  
516 observation is prominent in the Pacific (Fig. 5). The observed Pacific subsurface  $[I^-]$  peak mirrors the  $[IO_3^-]$  minima  
517 that occurs at depths where ODZs are present. This ODZ feature in the averaged Pacific observation profile is likely  
518 the result of sampling bias since most of the observations from the Pacific were from the ETNP (Rue et al., 1997;  
519 Moriyasu et al., 2020), thus not reflecting the overall iodine distribution in the Pacific Ocean (Fig. S8). As for the  
520 meridional trends, sampling bias is again demonstrated in a depth profiles masked to only include modeled grid points  
521 with corresponding observation data, with a clear mid-depth ODZ feature in the modeled Pacific depth profiles (Fig.  
522 S8). A similar example is from the Indian Ocean, which we do not show, since most iodine subsurface data come from  
523 the ODZ, not normal marine, localities. All this said, while the general features of iodine speciation with depth are  
524 generally similar, our data compilation indicates the potential for some basin-specific variations which require further  
525 research to validate and mechanistically understand.

#### 526 4.2.3. Iodine distribution within ODZs



527 One of the major goals of calibrating the iodine cycle in cGENIE is to simulate the iodine behavior associated with  
528 ancient low oxygen settings. To assess this potential, we analyzed model performance for the ETNP (Rue et al., 1997;  
529 Moriyasu et al., 2020) where observation data are abundant and the areal extent of the ODZ is sufficiently large to be  
530 reflected in the model grid (Fig. 6). Importantly, it should still be noted that cGENIE is best applied to understanding  
531 broad scale processes and thus the scope of the ETNP ODZ transect comparison is likely too fine resolution to expect  
532 a good match. That said, the simulated reduction in  $\text{IO}_3^-$  to  $\text{I}^-$  generally overlaps with the extent of the ODZ (Fig. 6),  
533 which provides support for the use of cGENIE to understand the broad distribution of ancient  $[\text{IO}_3^-]$  and  $[\text{O}_2]$ . Other  
534 non-threshold model parameterization-combinations (shown in Fig. S4) did not replicate the ODZ feature in iodine  
535 speciation.

536 Across all model configurations assuming cGENIE- $[\text{O}_2]$ , the prominent discrepancy is an underestimation of  
537 the spatial extent and intensity of the  $\text{IO}_3^-$  depletion zone in the ETNP (Fig. 6) because simulated subsurface  $\text{O}_2$   
538 deficient area is notably narrower than that compared to WOA climatology (Fig. 6, Fig. S5). There are multiple factors  
539 that might affect the performance of simulating the  $\text{O}_2$  cycle in cGENIE. The model might underestimate the intensity  
540 of gyres in the North and Tropical Pacific, resulting in the narrowed ODZs in these areas. Also, the pattern of upwelled  
541 nutrients into the surficial Tropical Pacific needs to be tuned to better replicate the productivity and the  $\text{O}_2$  consumption  
542 during remineralization. Another source of uncertainty is that the short-term processes, such as seasonal or El Niño  
543 driven ODZ variations at the time of sample collection are not replicated in the cGENIE simulations.

544 Other data-model misfits might have arisen as a result of additional  $\text{IO}_3^-$ -reduction dependencies not  
545 explicitly accounted for in the model. As discussed above, shipboard incubation and radiogenic-tracer-spiked rate  
546 calculation suggest that  $\text{IO}_3^-$  reduction is slow in the offshore ETNP ODZ (Hardisty et al., 2021). This could explain  
547 why measurable  $\text{IO}_3^-$  is present in the core of the ETNP ODZ (Fig. 6). This is further exacerbated in the Eastern  
548 Tropical South Pacific ODZ, where  $[\text{IO}_3^-]$  remains above 250 nM in some studies (Cutter et al., 2018) but near  
549 detection limits in others (Rapp et al., 2020), suggesting extreme spatiotemporal variability related to currently  
550 unconstrained factors. Further, while the capability of microbes using  $\text{IO}_3^-$  as an electron acceptor for oxidizing organic  
551 matter has been confirmed in laboratory culture experiments (Counsell et al., 1997; Reyes-Umana et al., 2021;  
552 Yamazaki et al., 2020; Amachi et al., 2007; Farrenkopf et al., 1997), no study to date has demonstrated non- $\text{O}_2$   
553 dependent controls driving variable  $\text{IO}_3^-$  reduction rates.

554 An important factor contributing to elevated  $[\text{I}^-]$  in ODZs is benthic fluxes and reduction occurring within  
555 the uppermost layers of marine sediments (akin to denitrification). To help account for this in our M score and model  
556 calibration (see: methods section), excess iodine was filtered from our observational dataset. The excess iodine  
557 originated from the sediment flux has been observed in ODZ water columns contacting anoxic sediments (Chapman,  
558 1983; Farrenkopf and Luther, 2002; Cutter et al., 2018; Moriyasu et al., 2020). We note that excess iodine is explicitly  
559 as  $\text{I}^-$ , reflecting the limited or lack of oxygen within the ODZ, and is a local-regional phenomenon not yet observed to  
560 persist beyond ODZ settings. As such, since our goal is a paleoceanography-focused model, cGENIE does not  
561 incorporate the benthic flux of  $\text{I}^-$  because only  $\text{IO}_3^-$  is tracked via the I:Ca paleoredox proxy.

562

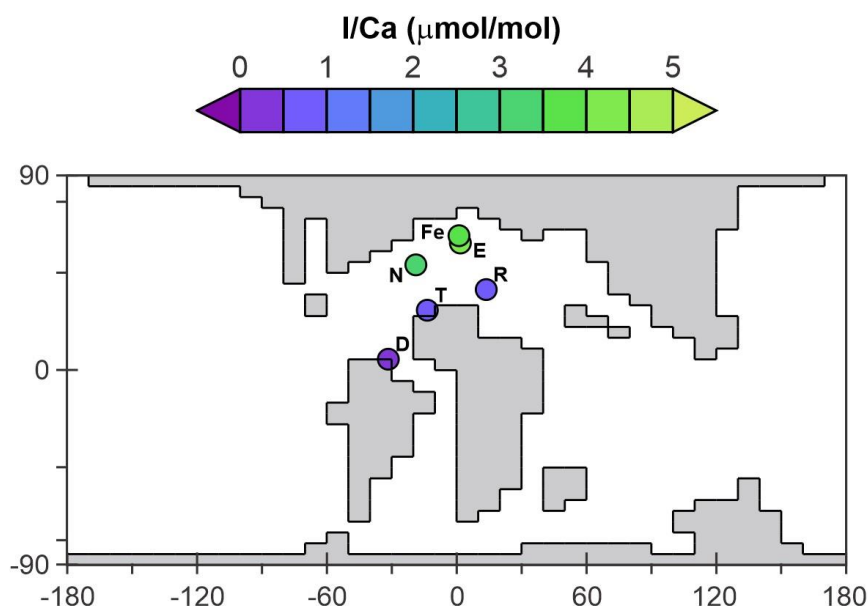
#### 563 4.3. Applicability of the cGENIE marine iodine cycle to paleo redox reconstruction



564 Parameter tuning, and the ability to reproduce modern observations, does not by itself offer any guarantee that spatial  
565 patterns are being simulated for the ‘correct’ reason (i.e., specific set and relative importance of mechanisms). This is  
566 even more pertinent in the context of the application of a modern-tuned model to paleo redox reconstruction. To test  
567 whether our new iodine cycle had predictive power in the geological past, we carried out a deep-time plausibility test.

568 For the paleo plausibility test, we adopted the Cretaceous, pre-OAE2 (ca. 93 Ma) configuration (continental  
569 arrangement and ocean bathymetry, wind stress and velocity, and zonal average planetary albedo boundary conditions)  
570 from Monteiro et al., (2012). We choose this particular geological interval because the controls on ocean redox have  
571 been previously evaluated using the GENIE model (Monteiro et al., 2012; Hülse et al., 2019), the oceanic conditions  
572 are much more extensively dysoxic and anoxic than present-day and hence represent a relatively severe test of the  
573 model iodine cycle, and a number of I:Ca proxy measurements are available (Zhou et al., 2015). In order to evaluate  
574 the same configuration of the iodine cycle as optimized in this study, we also substituted the temperature-independent  
575 representation of biological export production and fixed remineralization profile of POM in the water column (i.e.,  
576 Ridgwell et al., (2007)) for the temperature-dependent scheme of Crichton et al., (2021). However, in substituting the  
577 biological pump scheme in the model we change the ocean redox landscape compared with e.g., Monteiro et al., (2012).  
578 We therefore test a range of different assumptions regarding the ocean PO<sub>4</sub> inventory at the time as a means of  
579 generating a range of different plausible states of ocean oxygenation. In this, we test: 0.2, 0.4, 0.6, 0.8, 1.0, and 1.5  
580 times the mean modern concentration (2.15 mM). We run the model with each of the best-fit (highest M-score) sets  
581 of parameter values associated with the 5 different parameterization-combinations (but focus on the results of the same  
582 3 combinations we did for comparison against modern), and for each of the varying PO<sub>4</sub> inventory assumptions, for  
583 10,000 years to steady-state.

584



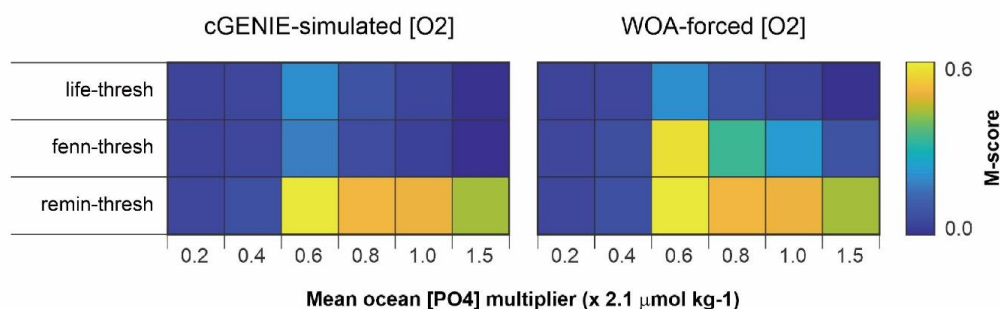
585

586 **Figure 7: The continental setting during the Cretaceous OAE2 (Cenomanian - Turonian) in cGENIE. The**  
587 **colored dots represent averaged pre-OAE2 I:Ca measurements from each of the sections. D = Demerara Rise;**  
588 **E = Eastbourne; Fe = South Ferriby; N = Newfoundland; R = Raia del Pedale; T = Tarfaya.**

589

590 The I:Ca data used for comparison with the model come from 6 sections (Zhou et al., 2015, Fig. 7, listed in  
591 Table S3). The pre-OAE2 I:Ca baseline value from each section is estimated through averaging the pre-CIE I:Ca  
592 measurements from Table S1 of Zhou et al., (2015). For quantitative comparison between the model and the I:Ca data,  
593 we create an empirically derived forward proxy model for I:Ca. In this, we took the simulated concentration of  $\text{IO}_3^-$   
594 and  $\text{Ca}^{2+}$  in the ocean surface layer of the model at every ocean grid point, and applied the temperature-dependent  
595 linear incorporation relationship derived from inorganic calcite synthesis experiment of Zhou et al., (2014), to estimate  
596 I:Ca. The converted modelled I:Ca at each section were then directly compared with the mean pre-OAE2 I:Ca  
597 measurements using the M score (Fig. 8). We then extracted simulated I:Ca values from the model grid points  
598 corresponding to the sections reported by Zhou et al., (2015) and calculated the M-score. The statistical results of this  
599 comparison are illustrated in Fig. 8 for the 3 parameterizations chosen for focus in the main text and for Fig. S9 for  
600 the full parameterization-combinations and for parameter calibrations derived from internally and WOA-forced  
601 dissolved oxygen distributions.

602



603

604 **Figure 8. The model skill scores of modeled and measured I:Ca during the pre-OAE2. The iodine cycling**  
 605 **parameters are derived from modern simulations with cGENIE-simulated [O<sub>2</sub>] and WOA-forced [O<sub>2</sub>],**  
 606 **respectively. lifetime-thresh = lifetime-threshold; remin-thresh +DOC = reminO2lifetime-threshold +DOC**  
 607 **remineralization; remin-thresh = reminO2lifetime-threshold; fenn-thresh = fennel-threshold; life-inhib =**  
 608 **lifetime-inhibition; life-remin +DOC = lifetime-reminSO4lifetime +DOC remineralization; life-remin =**  
 609 **lifetime-reminSO4lifetime.**

610

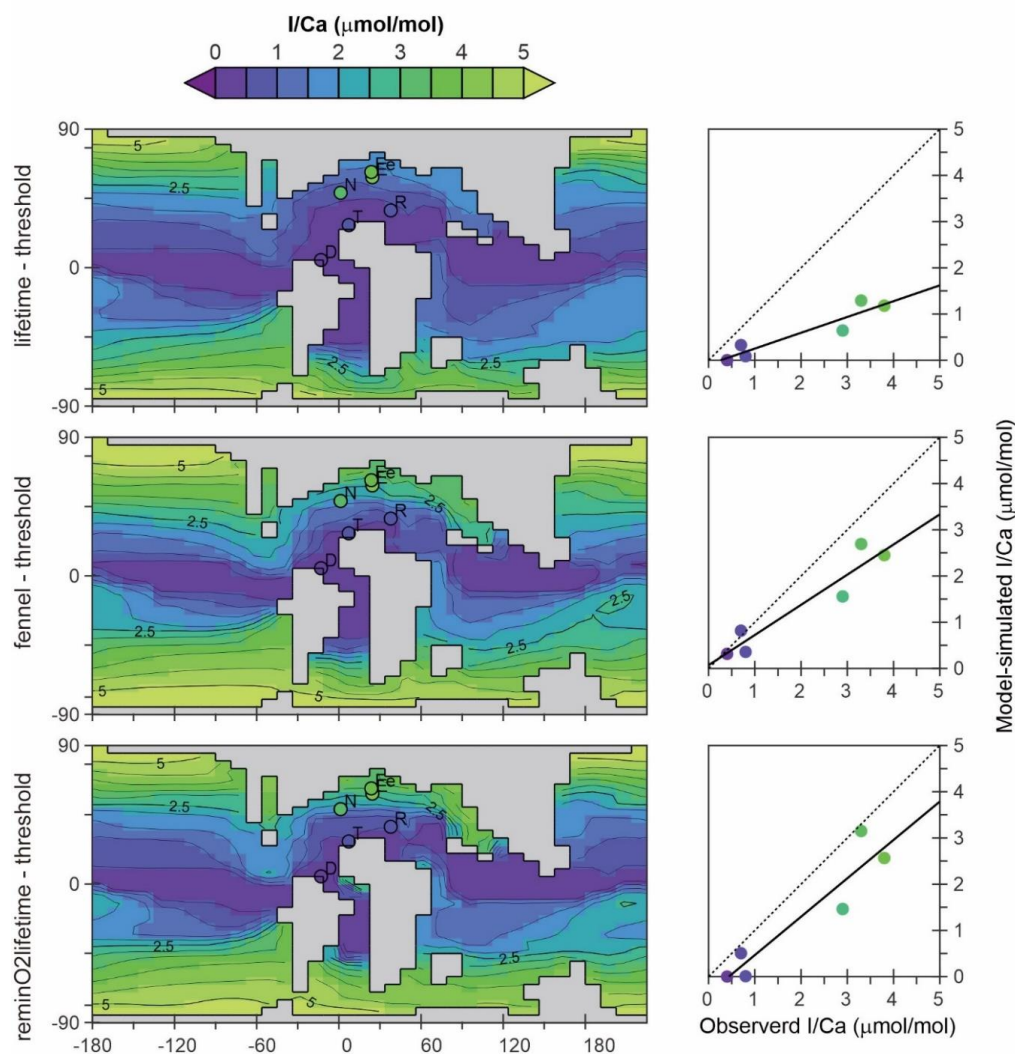
611 Most of the parameterization-combinations tested reach their highest M scores under the assumption of 0.6-  
 612 0.8 × modern [PO<sub>4</sub>] (Fig. S9). Previous analysis using the same climatological configuration of the GENIE model  
 613 indicated a PO<sub>4</sub> inventory of 1.0 x modern was most consistent with geological redox-related observations prior to  
 614 OAE2 (Monteiro et al., 2012). However, our assumption here of temperature-dependent POM export and  
 615 remineralization leads to higher export and shallower more intense ODZs compared to temperature-invariant  
 616 biological scheme (see: Crichton et al., (2021)). Hence, for a similar degree of ocean anoxia, we would expect the  
 617 need for a slightly lower nutrient inventory, as we indeed find.

618 In terms of the I:Ca M-score, we find the parameterization-combinations “reminO2lifetime-threshold” and  
 619 “fennel-threshold” better replicate the geological observations compared to the “lifetime-threshold”. In general,  
 620 WOA-derived parameter sets perform better than those derived from cGENIE-[O<sub>2</sub>], again hinting at the importance  
 621 of reducing the uncertainties in simulating the modern O<sub>2</sub> cycle in cGENIE. These observations are also largely  
 622 independent of the ocean PO<sub>4</sub> inventory assumption. Although combinations of parameterizations such as  
 623 “reminO2lifetime-threshold” with DOC remineralization, “lifetime-inhibition”, and “lifetime-reminSO4lifetime”,  
 624 also produce elevated M scores, these combinations do not perform well in replicating iodine gradients within the  
 625 modern ocean (Figs. S2-4). Thus, until there is a better mechanistic understanding of IO<sub>3</sub><sup>-</sup> reduction in the modern  
 626 ocean, the safest choice is arguably to apply the parameterization that best reproduces modern observations and hence  
 627 retain use of the “threshold” IO<sub>3</sub><sup>-</sup> reduction parameterization for paleo applications.

628 The pre-OAE2 comparison is revealing because it encapsulates a strong gradient between high and very low  
 629 I:Ca (Fig. 7), reflecting respectively, high and low surface ocean concentrations of IO<sub>3</sub><sup>-</sup> in the model. All three of the  
 630 parameterization-combinations we focus on here (with WOA-derived parameter values) correctly lead to very low  
 631 I:Ca values in the lower latitudinal sections (Demerara Rise, Tarfaya, and Raia del Pedale; Fig. 9), although with a  
 632 tendency to slightly overestimate seawater IO<sub>3</sub><sup>-</sup> depletion (cross-plots in Fig. 9). Low ocean surface [IO<sub>3</sub><sup>-</sup>] is due to



633 the existence of a circum-Equatorial band of intense sub-surface anoxia. In the higher latitudinal sections, including  
634 Newfoundland, Eastbourne, and South Ferriby, I:Ca values tend to be underestimated to varying degrees (Fig. 9).  
635 Compared to the “lifetime” parameterization, both “reminO2lifetime” and “fennel” oxidation simulate the I:Ca values  
636 in these high latitudinal sections rather better, with the regression closer to the 1:1 line (dotted in Fig. 9). We find this  
637 relationship instructional for understanding controls in the modern iodine cycle, which we discuss in more detail below.  
638



639

640 **Figure 9. The pre-OAE2 I:Ca field derived from cGENIE [IO<sub>3</sub><sup>-</sup>] simulations, and the comparison between**  
641 **modeled and observed I:Ca from sections.**

642





643 We first note that both ‘lifetime’ and ‘fennel’ iodine oxidation parameterizations in conjunction with a  
644 threshold of iodate reduction and internally generated GENIE-[O<sub>2</sub>], give rise to identical parameter values (Table 2).  
645 We infer that this is because the modern ocean is predominately well-oxygenated and hence there is little inhibition  
646 of I<sup>-</sup> oxidation in practice. In the Cretaceous environment, although I<sup>-</sup> oxidation inhibition should be widespread, the  
647 M-scores are similar (Fig. 8). The rate of I<sup>-</sup> oxidation in well oxygenated seawater is likely then critical in explaining  
648 elevated I:Ca values at higher Cretaceous latitudes. However, simply decreasing the lifetime in the modern ocean  
649 would result in an under estimation of surface ocean [I<sup>-</sup>]. The ‘fennel-threshold’ combination under WOA-[O<sub>2</sub>] reveals  
650 a trade-off that solves this—a decreased I<sup>-</sup> lifetime compensated for by increased rates of I<sup>-</sup> release to the ocean interior  
651 directly through the biological pump and elevated cellular I:C (3.5×10<sup>-4</sup> vs. 1.5×10<sup>-4</sup>). In the Cretaceous ocean this  
652 combination allows for both sharper latitudinal gradients in [IO<sub>3</sub><sup>-</sup>] (and hence I:Ca) to develop, as well as steeper  
653 vertical gradients which allow for non-zero I:Ca values at low latitudes to be captured (cross-plot in Fig. 9). This slight  
654 enhancement of the upper ocean [IO<sub>3</sub><sup>-</sup>] gradient is also apparent in the present-day analysis (Fig. 5). The combination  
655 of ‘reminO2lifetime’ with a reduction threshold works similarly—a shorter lifetime for I<sup>-</sup> under oxic conditions offset  
656 in the modern ocean by elevated cellular I:C (Table 2). However, in this case, our gridded parameter search identifies  
657 the trade-off as producing the highest M-score for both modelled and WOA oxygen distributions.

658 What we learn from this is that the cGENIE iodine cycle tuned to modern observations has predictive power  
659 under a very different state of ocean oxygenation (and circulation and operation of biological pump). However, this  
660 is not true for every choice of parameterization, and the simple ‘lifetime-threshold’ combination, which when  
661 calibrated was statistically almost the best representation of the iodine cycle, was unable to reproduce the latitudinal  
662 I:Ca gradients in the Cretaceous ocean. Shortening the lifetime (and adding an inhibition term) together with increasing  
663 the assumed cellular I:C, could maintain modern ocean fidelity whilst much better capturing Cretaceous I:Ca. That  
664 even better representations of Cretaceous I:Ca were possible but at the expense of reproducing modern observations  
665 adequately hints that improvements in our mechanistic understanding are needed, although all of the above assumes  
666 that the simulation of the Cretaceous redox landscape is plausible.

## 667 5. Conclusions

668 Using the cGENIE Earth system model, we performed a series of ensemble experiment parameter searches for suitable  
669 parameterizations to represent the marine iodine cycle and identified the best performing parameter value  
670 combinations in each case. We found that the optimized parameters associated with IO<sub>3</sub><sup>-</sup> planktonic uptake, water  
671 column IO<sub>3</sub><sup>-</sup> reduction and I<sup>-</sup> oxidation are within the range of field and experiment observations and hence plausible.  
672 Three iodine cycling parameter combinations, “lifetime-threshold”, “reminO2lifetime-threshold”, and “fennel-  
673 threshold” emerged as viable candidates following our tests of the global ocean model M score, and model-data  
674 comparison across specific iodine gradients (euphotic latitudinal distribution, depth distribution, and ODZ  
675 distribution). We further evaluate the plausibility of our parameterizations and their paleo and ocean deoxygenation  
676 applicability by contrasting forward-proxy model generated I:Ca values against observations, taking the (pre-OAE2)  
677 Cretaceous redox landscape as a case study. While some model-data discrepancies emerge for both modern and paleo,  
678 these highlight that future observational and/or experimental work is necessary to better constrain modern iodine



679 cycling mechanisms and related spatiotemporal heterogeneities. While we further identified the importance of  
680 improving the simulation of dissolved oxygen distributions in models, equally, we found that our conclusions  
681 regarding preferred parameterizations and even specific parameter values, was not overly dependent on the specific  
682 details of the simulated modern OMZs. Overall, our analysis gives us a degree of confidence that carbonate I:Ca ratios  
683 can be interpreted in terms of past ocean oxygenation using models such as 'cGENIE'.  
684



685 **Competing interests.** *The contact author has declared that none of the authors has any competing interests.*

686

687 **Author contributions.** *KC, AR, and DH conceptualized the research presented in this paper. DH and AR acquired*  
688 *funding to support the study. AR developed iodine tracer and associated biogeochemical mechanisms in cGENIE. KC*  
689 *and DH designed model performance under the modern ocean configurations. KC compiled the modern ocean iodine*  
690 *database and the Cretaceous I:Ca data. KC ran the modern-ocean cGENIE analysis and performed model-data*  
691 *comparison. AR performed model-data evaluation for Cretaceous configurations. KC prepared the manuscript with*  
692 *contributions from all co-authors.*

693

694 **Acknowledgements.** *Funding support for DH and KC comes from NSF OCE 1829406. AR acknowledges support from*  
695 *National Science Foundation grant EAR-2121165 and the NASA Interdisciplinary Consortia for Astrobiology*  
696 *Research (ICAR) Program (80NSSC21K0594).*

697

698 **Code availability.** *The code for the version of the ‘muffin’ release of the cGENIE Earth system model used in this*  
699 *paper, is tagged as v0.9.13, and is assigned a DOI: 10.5281/zenodo.3999080.*

700 *Configuration files for the specific experiments presented in the paper can be found in the directory: genie-*  
701 *userconfigs/PUBS/chengetal.BG.2020. Details of the experiments, plus the command line needed to run each one, are*  
702 *given in the readme.txt file in that directory. All other configuration files and boundary conditions are provided as*  
703 *part of the code release.*

704 *A manual detailing code installation, basic model configuration, tutorials covering various aspects of model*  
705 *configuration, experimental design, and output, plus the processing of results, is assigned a DOI:*  
706 *10.5281/zenodo.4305997.*

## 707 **References**

708 Amachi, S., Kawaguchi, N., Muramatsu, Y., Tsuchiya, S., Watanabe, Y., Shinoyama, H., and Fujii, T.: Dissimilatory  
709 iodate reduction by marine *Pseudomonas* sp. strain SCT, *Appl. Environ. Microbiol.*, 73, 5725–5730,  
710 <https://doi.org/10.1128/AEM.00241-07>, 2007.

711 Boscolo-Galazzo, F., Crichton, K. A., Ridgwell, A., Mawbey, E. M., Wade, B. S., and Pearson, P. N.: Temperature  
712 controls carbon cycling and biological evolution in the ocean twilight zone, *Science* (80-. ), 371, 1148–1152,  
713 <https://doi.org/10.1126/science.abb6643>, 2021.

714 Bowman, C. N., Lindskog, A., Kozik, N. P., Richbourg, C. G., Owens, J. D., and Young, S. A.: Integrated sedimentary,  
715 biotic, and paleoredox dynamics from multiple localities in southern Laurentia during the late Silurian (Ludfordian)  
716 extinction event, *Palaeogeogr. Palaeoclimatol. Palaeoecol.*, 553, 109799,  
717 <https://doi.org/10.1016/j.palaeo.2020.109799>, 2020.

718 Broecker, W. S. and Peng, T. H.: Tracers in the Sea., [https://doi.org/10.1016/0016-7037\(83\)90075-3](https://doi.org/10.1016/0016-7037(83)90075-3), 1983.

719 Campos, M. L. A. M., Farrenkopf, A. M., Jickells, T. D., and Luther, G. W.: A comparison of dissolved iodine cycling  
720 at the Bermuda Atlantic Time-series station and Hawaii Ocean Time-series station, *Deep. Res. Part II Top. Stud.*



- 721 Oceanogr., 43, 455–466, [https://doi.org/10.1016/0967-0645\(95\)00100-x](https://doi.org/10.1016/0967-0645(95)00100-x), 1996.
- 722 Cao, L., Eby, M., Ridgwell, A., Caldeira, K., Archer, D., Ishida, A., Joos, F., Matsumoto, K., and Mikolajewicz, U.:  
723 The role of ocean transport in the uptake of anthropogenic CO<sub>2</sub>, *Biogeosciences*, 375–390, 2009.
- 724 Chance, R., Weston, K., Baker, A. R., Hughes, C., Malin, G., Carpenter, L., Meredith, M. P., Clarke, A., Jickells, T.,  
725 D., Mann, P., and Rossetti, H.: Seasonal and interannual variation of dissolved iodine speciation at a coastal Antarctic  
726 site, *Mar. Chem.*, 118, 171–181, <https://doi.org/10.1016/j.marchem.2009.11.009>, 2010.
- 727 Chance, R., Baker, A. R., Carpenter, L., and Jickells, T. D.: The distribution of iodide at the sea surface, *Environ. Sci.*  
728 *Process. Impacts*, 16, 1841–1859, <https://doi.org/10.1039/c4em00139g>, 2014.
- 729 Chance, R., Tinel, L., Sherwen, T., Baker, A., Bell, T., Brindle, J., Campos, M., Croot, P., Ducklow, H., He, P.,  
730 Hoogakker, B., Hopkins, F., Hughes, C., Jickells, T., Loades, D., Reyes Macaya, D., Mahajan, A., Malin, G., Phillips,  
731 D., Sinha, A., Sarkar, A., Roberts, I., Roy, R., Song, X., Winklebauer, H., Wuttig, K., Yang, M., Zhou, P., and  
732 Carpenter, L.: Global sea-surface iodide observations, 1967–2018., [https://doi.org/doi:10.5285/7e77d6b9-83fb-41e0-](https://doi.org/doi:10.5285/7e77d6b9-83fb-41e0-e053-6c86abc069d0)  
733 [e053-6c86abc069d0](https://doi.org/doi:10.5285/7e77d6b9-83fb-41e0-e053-6c86abc069d0), 2019.
- 734 Chapman, P.: Changes in iodine speciation in the Benguela current upwelling system, *Deep Sea Res. Part A, Oceanogr.*  
735 *Res. Pap.*, 30, 1247–1259, [https://doi.org/10.1016/0198-0149\(83\)90083-3](https://doi.org/10.1016/0198-0149(83)90083-3), 1983.
- 736 Councell, T. B., Landa, E. R., and Lovley, D. R.: Microbial reduction of iodate, *Water. Air. Soil Pollut.*, 100, 99–106,  
737 1997.
- 738 Crichton, K. A., Wilson, J. D., Ridgwell, A., and Pearson, P. N. P. N.: Calibration of temperature-dependent ocean  
739 microbial processes in the cGENIE.muffin (v0.9.13) Earth system model, *Geosci. Model Dev.*, 14, 125–149,  
740 <https://doi.org/10.5194/gmd-14-125-2021>, 2021.
- 741 Cutter, G. A., Moffett, J. G., Nielsdóttir, M. C., and Sanial, V.: Multiple oxidation state trace elements in suboxic  
742 waters off Peru: In situ redox processes and advective/diffusive horizontal transport, *Mar. Chem.*, 201, 77–89,  
743 <https://doi.org/10.1016/j.marchem.2018.01.003>, 2018.
- 744 Dalsgaard, T., Stewart, F. J., Thamdrup, B., De Brabandere, L., Revsbech, N. P., Ulloa, O., Canfield, D. E., and  
745 Delong, E. F.: Oxygen at nanomolar levels reversibly suppresses process rates and gene expression in anammox and  
746 denitrification in the oxygen minimum zone off Northern Chile, *MBio*, 5, 1–14, [https://doi.org/10.1128/mBio.01966-](https://doi.org/10.1128/mBio.01966-14)  
747 [14](https://doi.org/10.1128/mBio.01966-14), 2014.
- 748 Ding, Y., Sun, W., Liu, S., Xie, J., Tang, D., Zhou, X., Zhou, L., Li, Z., Song, J., Li, Z., Xu, H., Tang, P., Liu, K., Li,  
749 W., and Chen, D.: Low oxygen levels with high redox heterogeneity in the late Ediacaran shallow ocean: Constraints  
750 from I/(Ca + Mg) and Ce/Ce\* of the Dengying Formation, South China, *Geobiology*, 20, 790–809,  
751 <https://doi.org/10.1111/gbi.12520>, 2022.
- 752 Edwards, A. and Truesdale, V. W.: Regeneration of inorganic iodine species in loch etive, a natural leaky incubator,  
753 *Estuar. Coast. Shelf Sci.*, 45, 357–366, <https://doi.org/10.1006/ecss.1996.0185>, 1997.
- 754 Edwards, C. T., Fike, D. A., Saltzman, M. R., Lu, W., and Lu, Z.: Evidence for local and global redox conditions at  
755 an Early Ordovician (Tremadocian) mass extinction, *Earth Planet. Sci. Lett.*, 481, 125–135,  
756 <https://doi.org/10.1016/j.epsl.2017.10.002>, 2018.
- 757 Edwards, N. R. and Marsh, R.: Uncertainties due to transport-parameter sensitivity in an efficient 3-D ocean-climate



- 758 model, *Clim. Dyn.*, 415–433, <https://doi.org/10.1007/s00382-004-0508-8>, 2005.
- 759 Elderfield, H. and Truesdale, V. W.: On the biophilic nature of iodine in seawater, *Earth Planet. Sci. Lett.*, 50, 105–  
760 114, [https://doi.org/10.1016/0012-821X\(80\)90122-3](https://doi.org/10.1016/0012-821X(80)90122-3), 1980.
- 761 Fang, H., Tang, D., Shi, X., Zhou, L., Zhou, X., Wu, M., Song, H., and Riding, R.: Early Mesoproterozoic Ca-  
762 carbonate precipitates record fluctuations in shallow marine oxygenation, *Precambrian Res.*, 373, 106630,  
763 <https://doi.org/10.1016/j.precamres.2022.106630>, 2022.
- 764 Farrenkopf, A. M. and Luther, G. W.: Iodine chemistry reflects productivity and denitrification in the Arabian Sea:  
765 Evidence for flux of dissolved species from sediments of western India into the OMZ, *Deep. Res. Part II Top. Stud.*  
766 *Oceanogr.*, 49, 2303–2318, [https://doi.org/10.1016/S0967-0645\(02\)00038-3](https://doi.org/10.1016/S0967-0645(02)00038-3), 2002.
- 767 Farrenkopf, A. M., Dollhopf, M. E., Chadhain, S. N., Luther, G. W., and Nealson, K. H.: Reduction of iodate in  
768 seawater during Arabian Sea shipboard incubations and in laboratory cultures of the marine bacterium *Shewanella*  
769 *putrefaciens* strain MR-4, *Mar. Chem.*, 57, 347–354, [https://doi.org/10.1016/S0304-4203\(97\)00039-X](https://doi.org/10.1016/S0304-4203(97)00039-X), 1997.
- 770 Fennel, K., Follows, M., and Falkowski, P. G.: The co-evolution of the nitrogen, carbon and oxygen cycles in the  
771 Proterozoic ocean, *Am. J. Sci.*, 305, 526–545, 2005.
- 772 Garcia, H. E., Weathers, K., Paver, C. R., Smolyar, I., Boyer, T. P., Locarnini, R. A., Zweng, M. M., Mishonov, A.  
773 V., Baranova, O. K., Seidov, D., and Reagan, J. R.: Volume 3: Dissolved Oxygen, Apparent Oxygen Utilization, and  
774 Oxygen Saturation. A. Mishonov Technical Ed.; NOAA Atlas NESDIS 83, World Ocean Atlas 2018, 38 pp., 2018.
- 775 Hardisty, D. S., Lu, Z., Planavsky, N. J., Bekker, A., Philippot, P., Zhou, X., and Lyons, T. W.: An iodine record of  
776 Paleoproterozoic surface ocean oxygenation, *Geology*, 42, 619–622, <https://doi.org/10.1130/G35439.1>, 2014.
- 777 Hardisty, D. S., Horner, T. J., Wankel, S. D., Blusztajn, J., and Nielsen, S. G.: Experimental observations of marine  
778 iodide oxidation using a novel sparge-interface MC-ICP-MS technique, *Chem. Geol.*, 532, 119360,  
779 <https://doi.org/10.1016/j.chemgeo.2019.119360>, 2020.
- 780 Hardisty, D. S., Horner, T. J., Evans, N., Moriyasu, R., Babbitt, A. R., Wankel, S. D., Moffett, J. W., and Nielsen, S.  
781 G.: Limited iodate reduction in shipboard seawater incubations from the Eastern Tropical North Pacific oxygen  
782 deficient zone, *Earth Planet. Sci. Lett.*, 554, 116676, <https://doi.org/10.1016/j.epsl.2020.116676>, 2021.
- 783 Hashim, M. S., Burke, J. E., Hardisty, D. S., and Kaczmarek, S. E.: Iodine incorporation into dolomite: Experimental  
784 constraints and implications for the iodine redox proxy and Proterozoic Ocean, *Geochim. Cosmochim. Acta*, 338,  
785 365–381, <https://doi.org/10.1016/j.gca.2022.10.027>, 2022.
- 786 He, P., Hou, X., and Aldahan, A.: Iodine isotopes species fingerprinting environmental conditions in surface water  
787 along the northeastern Atlantic Ocean, *Sci. Rep.*, 3, 1–9, <https://doi.org/10.1038/srep02685>, 2013.
- 788 Hepach, H., Hughes, C., Hogg, K., Collings, S., and Chance, R.: Senescence as the main driver of iodide release from  
789 a diverse range of marine phytoplankton, *Biogeosciences*, 17, 2453–2471, <https://doi.org/10.5194/bg-17-2453-2020>,  
790 2020.
- 791 Hughes, C., Barton, E., Hepach, H., Chance, R., Wadley, M. R., Pickering, M. D., Hogg, K., Pommerening-r, A.,  
792 Stevens, D. P., and Jickells, T. D.: Oxidation of iodide to iodate by cultures of marine ammonia-oxidising bacteria,  
793 *Mar. Chem.*, 234, <https://doi.org/10.1016/j.marchem.2021.104000>, 2021.
- 794 Hülse, D., Arndt, S., and Ridgwell, A.: Mitigation of Extreme Ocean Anoxic Event Conditions by Organic Matter



- 795 Sulfurization, *Paleoceanogr. Paleoclimatology*, 34, 476–489, <https://doi.org/10.1029/2018PA003470>, 2019.
- 796 Jia-zhong, Z. and Whitfield, M.: KINETICS OF INORGANIC REDOX REACTIONS IN SEAWATER I . The  
797 reduction of iodate by bisulphide Micro-organisms play a dominant role in the diagenesis of organic-rich sediments .  
798 The oxidative breakdown of the organic matter , with the accom- panying reductio, *Science (80-. )*, 19, 121–137,  
799 1986.
- 800 Jiang, Z., Cui, M., Qian, L., Jiang, Y., Shi, L., Dong, Y., Li, J., and Wang, Y.: Abiotic and Biotic Reduction of Iodate  
801 Driven by *Shewanella oneidensis* MR-1 , *Environ. Sci. Technol.*, <https://doi.org/10.1021/acs.est.3c06490>, 2023.
- 802 Kerisit, S. N., Smith, F. N., Saslow, S. A., Hoover, M. E., Lawter, A. R., and Qafoku, N. P.: Incorporation Modes of  
803 Iodate in Calcite, *Environ. Sci. Technol.*, 52, 5902–5910, <https://doi.org/10.1021/acs.est.8b00339>, 2018.
- 804 Laws, E. A., Falkowski, P. G., Smith, W. O., Ducklow, H., and James J McCarthy: Temperature effects on export  
805 production in the open ocean, *Global Biogeochem. Cycles*, 14, 1231–1246, 2000.
- 806 Liu, A., Tang, D., Shi, X., Zhou, X., Zhou, L., Shang, M., Li, Y., and Fang, H.: Mesoproterozoic oxygenated deep  
807 seawater recorded by early diagenetic carbonate concretions from the Member IV of the Xiamaling Formation, North  
808 China, *Precambrian Res.*, 341, 105667, <https://doi.org/10.1016/j.precamres.2020.105667>, 2020.
- 809 Lu, W., Ridgwell, A., Thomas, E., Hardisty, D. S., Luo, G., Algeo, T. J., Saltzman, M. R., Gill, B. C., Shen, Y., Ling,  
810 H. F., Edwards, C. T., Whalen, M. T., Zhou, X., Gutchess, K. M., Jin, L., Rickaby, R. E. M., Jenkyns, H. C., Lyons,  
811 T. W., Lenton, T. M., Kump, L. R., and Lu, Z.: Late inception of a resiliently oxygenated upper ocean, *Science (80-. )*,  
812 361, 174–177, <https://doi.org/10.1126/science.aar5372>, 2018.
- 813 Lu, W., Rickaby, R. E. M., Hoogakker, B. A. A., Rathburn, A. E., Burkett, A. M., Dickson, A. J., Martínez-Méndez,  
814 G., Hillenbrand, C. D., Zhou, X., Thomas, E., and Lu, Z.: I/Ca in epifaunal benthic foraminifera: A semi-quantitative  
815 proxy for bottom water oxygen in a multi-proxy compilation for glacial ocean deoxygenation, *Earth Planet. Sci. Lett.*,  
816 533, <https://doi.org/10.1016/j.epsl.2019.116055>, 2020a.
- 817 Lu, W., Dickson, A. J., Thomas, E., Rickaby, R. E. M., Chapman, P., and Lu, Z.: Refining the planktic foraminiferal  
818 I/Ca proxy: Results from the Southeast Atlantic Ocean, *Geochim. Cosmochim. Acta*, 287, 318–327,  
819 <https://doi.org/10.1016/j.gca.2019.10.025>, 2020b.
- 820 Lu, Z., Jenkyns, H. C., and Rickaby, R. E. M.: Iodine to calcium ratios in marine carbonate as a paleo-redox proxy  
821 during oceanic anoxic events, *Geology*, 38, 1107–1110, <https://doi.org/10.1130/G31145.1>, 2010.
- 822 Lu, Z., Hoogakker, B. A. A., Hillenbrand, C.-D., Zhou, X., Thomas, E., Gutchess, K. M., Lu, W., Jones, L., and  
823 Rickaby, R. E. M.: Oxygen depletion recorded in upper waters of the glacial Southern Ocean, *Nat. Commun.*, 7, 1–8,  
824 <https://doi.org/10.1038/ncomms11146>, 2016.
- 825 Luther, G. W.: Review on the physical chemistry of iodine transformations in the oceans, *Front. Mar. Sci.*, 10, 1–16,  
826 <https://doi.org/10.3389/fmars.2023.1085618>, 2023.
- 827 Luther, G. W. and Campbell, T.: Iodine speciation in the water column of the Black Sea, *Deep Sea Res. Part A*.  
828 *Oceanogr. Res. Pap.*, 38, S875–S882, [https://doi.org/10.1016/s0198-0149\(10\)80014-7](https://doi.org/10.1016/s0198-0149(10)80014-7), 1991.
- 829 Luther, G. W., Wu, J., and Cullen, J. B.: Redox Chemistry of Iodine in Seawater, *Adv. Chem.*, 135–155, 1995.
- 830 Luther, W.: Iodine Chemistry in the Water the Chesapeake Bay : Evidence Iodine Forms Column of for Organic,  
831 *Esruarine, Coast. Shelf Sci.*, 32, 267–279, 1991.





- 832 Lyons, T. W., Reinhard, C. T., and Planavsky, N. J.: The rise of oxygen in Earth's early ocean and atmosphere, *Nature*,  
833 506, 307–315, <https://doi.org/10.1038/nature13068>, 2014.
- 834 Marsh, R., Müller, S. A., Yool, A., and Edwards, N. R.: Incorporation of the C-GOLDSTEIN efficient climate model  
835 into the GENIE framework: &quot;eb\_go\_gs&quot;; configurations of GENIE, *Geosci. Model Dev.*, 4, 957–992,  
836 <https://doi.org/10.5194/gmd-4-957-2011>, 2011.
- 837 Martin, T. S., Primeau, F., and Casciotti, K. L.: Modeling oceanic nitrate and nitrite concentrations and isotopes using  
838 a 3-D inverse N cycle model, *Biogeosciences*, 347–367, 2019.
- 839 Matsumoto, K.: Radiocarbon-based circulation age of the world oceans, *J. Geophys. Res. Ocean.*, 112, 1–7,  
840 <https://doi.org/10.1029/2007JC004095>, 2007.
- 841 Monteiro, F. M., Pancost, R. D., Ridgwell, A., and Donnadieu, Y.: Nutrients as the dominant control on the spread of  
842 anoxia and euxinia across the Cenomanian-Turonian oceanic anoxic event (OAE2): Model-data comparison,  
843 *Paleoceanography*, 27, <https://doi.org/10.1029/2012PA002351>, 2012.
- 844 Moriyasu, R., Evans, N., Bolster, K. M., Hardisty, D. S., and Moffett, J. W.: The Distribution and Redox Speciation  
845 of Iodine in the Eastern Tropical North Pacific Ocean, *Global Biogeochem. Cycles*, 34, 1–23,  
846 <https://doi.org/10.1029/2019GB006302>, 2020.
- 847 Moriyasu, R., Bolster, K. M., Hardisty, D. S., Kadko, D. C., Stephens, M. P., and Moffett, J. W.: Meridional survey  
848 of the Central Pacific reveals iodide accumulation in equatorial surface waters and benthic sources in the abyssal plain,  
849 *Global Biogeochem. Cycles*, <https://doi.org/10.1029/2021GB007300>, 2023.
- 850 Podder, J., Lin, J., Sun, W., Botis, S. M., Tse, J., Chen, N., Hu, Y., Li, D., Seaman, J., and Pan, Y.: Iodate in calcite  
851 and vaterite: Insights from synchrotron X-ray absorption spectroscopy and first-principles calculations, *Geochim.*  
852 *Cosmochim. Acta*, 198, 218–228, <https://doi.org/10.1016/j.gca.2016.11.032>, 2017.
- 853 Pohl, A., Lu, Z., Lu, W., Stockey, R. G., Elrick, M., Li, M., Desrochers, A., Shen, Y., He, R., Finnegan, S., and  
854 Ridgwell, A.: Vertical decoupling in Late Ordovician anoxia due to reorganization of ocean circulation, *Nat. Geosci.*,  
855 14, 868–873, <https://doi.org/10.1038/s41561-021-00843-9>, 2021.
- 856 Pohl, A., Ridgwell, A., Stockey, R. G., Thomazo, C., Keane, A., Vennin, E., and Scotese, C. R.: Continental  
857 configuration controls ocean oxygenation during the Phanerozoic, *Nature*, 608, 523–527,  
858 <https://doi.org/10.1038/s41586-022-05018-z>, 2022.
- 859 Rapp, I., Schlosser, C., Barraqueta, J. M., Wenzel, B., Lüdke, J., and Scholten, J.: Controls on redox-sensitive trace  
860 metals in the Mauritanian oxygen minimum zone, 4157–4182, 2019.
- 861 Rapp, I., Schlosser, C., Browning, T. J., Wolf, F., Le Moigne, F. A. C., Gledhill, M., and Achterberg, E. P.: El Niño-  
862 Driven Oxygenation Impacts Peruvian Shelf Iron Supply to the South Pacific Ocean, *Geophys. Res. Lett.*, 47,  
863 <https://doi.org/10.1029/2019GL086631>, 2020.
- 864 Reinhard, C. T. and Planavsky, N. J.: The History of Ocean Oxygenation, *Ann. Rev. Mar. Sci.*, 14, 331–353,  
865 <https://doi.org/10.1146/annurev-marine-031721-104005>, 2022.
- 866 Reinhard, C. T., Planavsky, N. J., Olson, S. L., Lyons, T. W., and Erwin, D. H.: Earth's oxygen cycle and the evolution  
867 of animal life, *Proc. Natl. Acad. Sci. U. S. A.*, 113, 8933–8938, <https://doi.org/10.1073/pnas.1521544113>, 2016.
- 868 Reinhard, C. T., Olson, S. L., Turner, S. K., Päläike, C., Kanzaki, Y., and Ridgwell, A.: Oceanic and atmospheric



- 869 methane cycling in the cGENIE Earth system model, *Geosci. Model Dev.*, 1–45, <https://doi.org/10.5194/gmd-2020->  
870 32, 2020.
- 871 Remmelzwaal, S. R. C., Dixon, S., Parkinson, I. J., Schmidt, D. N., Monteiro, F. M., Sexton, P., Fehr, M. A., Peacock,  
872 C., Donnadieu, Y., and James, R. H.: Investigating Ocean Deoxygenation During the PETM Through the Cr Isotopic  
873 Signature of Foraminifera, *Paleoceanogr. Paleoclimatology*, 34, 917–929, <https://doi.org/10.1029/2018PA003372>,  
874 2019.
- 875 Reyes-Umana, V., Henning, Z., Lee, K., Barnum, T. P., and Coates, J. D.: Genetic and phylogenetic analysis of  
876 dissimilatory iodate-reducing bacteria identifies potential niches across the world’s oceans, *ISME J.*,  
877 <https://doi.org/10.1038/s41396-021-01034-5>, 2021.
- 878 Ridgwell, A., Hargreaves, J. C., Edwards, N. R., Annan, J. D., Lenton, T. M., Marsh, R., Yool, A., and Watson, A. A.:  
879 Marine geochemical data assimilation in an efficient Earth system model of global biogeochemical cycling,  
880 *Biogeosciences*, 4, 87–104, <https://doi.org/10.5194/bg-4-87-2007>, 2007.
- 881 Rue, E. L., Smith, G. J., Cutter, G. A., and Bruland, K. W.: The response of trace element redox couples to suboxic  
882 conditions in the water column, *Deep. Res. Part I Oceanogr. Res. Pap.*, 44, 113–134, <https://doi.org/10.1016/S0967->  
883 0637(96)00088-X, 1997.
- 884 Schnur, A. A., Sutherland, K. M., Hansel, C. M., and Hardisty, D. S.: Rates and pathways of iodine speciation  
885 transformations at the Bermuda Atlantic Time Series, *Front. Mar. Sci.*, 1–14,  
886 <https://doi.org/10.3389/fmars.2023.1272870>, 2024.
- 887 Shang, M., Tang, D., Shi, X., Zhou, L., Zhou, X., Song, H., and Jiang, G.: A pulse of oxygen increase in the early  
888 Mesoproterozoic ocean at ca. 1.57–1.56 Ga, *Earth Planet. Sci. Lett.*, 527, 115797,  
889 <https://doi.org/10.1016/j.epsl.2019.115797>, 2019.
- 890 Sherwen, T., Chance, R. J., Tinel, L., Ellis, D., Evans, M. J., and Carpenter, L. J.: A machine-learning-based global  
891 sea-surface iodide distribution, *Earth Syst. Sci. Data*, 11, 1239–1262, 2019.
- 892 Ştreangă, I.-M., Repeta, D. J., Blusztajn, J. S., and Horner, T. J.: Speciation and cycling of iodine in the subtropical  
893 North Pacific Ocean, *Front. Mar. Sci.*, 1–15, <https://doi.org/10.3389/fmars.2023.1272968>, 2024.
- 894 Tang, D., Fang, H., Shi, X., Liang, L., Zhou, L., Xie, B., Huang, K., Zhou, X., Wu, M., and Riding, R.:  
895 Mesoproterozoic Molar Tooth Structure Related to Increased Marine Oxygenation, *J. Geophys. Res. Biogeosciences*,  
896 128, 1–18, <https://doi.org/10.1029/2022jg007077>, 2023.
- 897 Thamdrup, B., Dalsgaard, T., and Revsbech, N. P.: Widespread functional anoxia in the oxygen minimum zone of the  
898 Eastern South Pacific, *Deep. Res. Part I Oceanogr. Res. Pap.*, 65, 36–45, <https://doi.org/10.1016/j.dsr.2012.03.001>,  
899 2012.
- 900 Truesdale, V. W., Bale, A. J., and Woodward, E. M. S.: The meridional distribution of dissolved iodine in near-surface  
901 waters of the Atlantic Ocean, *Prog. Oceanogr.*, 45, 387–400, [https://doi.org/10.1016/S0079-6611\(00\)00009-4](https://doi.org/10.1016/S0079-6611(00)00009-4), 2000.
- 902 Truesdale, V. W., Watts, S. F., and Rendell, A. R.: On the possibility of iodide oxidation in the near-surface of the  
903 Black Sea and its implications to iodine in the general ocean, *Deep. Res. Part I*, 48, 2397–2412, 2001.
- 904 Truesdale, V. W., Nausch, G., and Waite, T. J.: The effects of the 2001 Barotropic intrusion of bottom-water upon the  
905 vertical distribution of inorganic iodine in the Gotland Deep, *Cont. Shelf Res.*, 55, 155–167,



- 906 <https://doi.org/10.1016/j.csr.2013.01.005>, 2013.
- 907 Tsunogai, S.: Iodine in the deep water of the ocean, *Deep. Res.*, 18, 913–919, 1971.
- 908 Uahengo, C. I., Shi, X., Jiang, G., and Vatuva, A.: Transient shallow-ocean oxidation associated with the late  
909 Ediacaran Nama skeletal fauna: Evidence from iodine contents of the Lower Nama Group, southern Namibia,  
910 *Precambrian Res.*, 343, 105732, <https://doi.org/10.1016/j.precamres.2020.105732>, 2020.
- 911 Wadley, M. R., Stevens, D. P., Jickells, T. D., Hughes, C., Chance, R., Hepach, H., Tinel, L., and Carpenter, L. J.: A  
912 Global Model for Iodine Speciation in the Upper Ocean, *Global Biogeochem. Cycles*, 34, 0–3,  
913 <https://doi.org/10.1029/2019GB006467>, 2020.
- 914 Watterson, I. G.: Non-dimensional measures of climate model performance, *Int. J. Climatol.*, 16, 379–391,  
915 [https://doi.org/10.1002/\(SICI\)1097-0088\(199604\)16:4<379::AID-JOC18>3.0.CO;2-U](https://doi.org/10.1002/(SICI)1097-0088(199604)16:4<379::AID-JOC18>3.0.CO;2-U), 1996.
- 916 Wei, B., Tang, D., Shi, X., Lechte, M., Zhou, L., Zhou, X., and Song, H.: A Pulsed Oxygenation in Terminal  
917 Paleoproterozoic Ocean: Evidence From the Transition Between the Chuanlinggou and Tuanshanzi Formations, North  
918 China, *Geochemistry, Geophys. Geosystems*, 22, 1–23, <https://doi.org/10.1029/2020GC009612>, 2021.
- 919 Wong, G. T. F. and Brewer, P. G.: The marine chemistry of iodine in anoxic basins, *Geochim. Cosmochim. Acta*, 41,  
920 151–159, [https://doi.org/10.1016/0016-7037\(77\)90195-8](https://doi.org/10.1016/0016-7037(77)90195-8), 1977.
- 921 Wong, G. T. F., Takayanagi, K., and Todd, J. F.: Dissolved iodine in waters overlying and in the Orca Basin, Gulf of  
922 Mexico, *Mar. Chem.*, 17, 177–183, [https://doi.org/10.1016/0304-4203\(85\)90072-6](https://doi.org/10.1016/0304-4203(85)90072-6), 1985.
- 923 Wong, G. T. F., Piumsomboon, A. U., Dunstan, W. M., Wong, G. T. F., Piumsomboon, A. U., and Dunstan, W. M.:  
924 The transformation of iodate to iodide in marine phytoplankton cultures, *Mar. Geol. Prog. Ser.*, 237, 27–39, 2002.
- 925 Yamazaki, C., Kashiwa, S., Horiuchi, A., and Kasahara, Y.: A novel dimethylsulfoxide reductase family of  
926 molybdenum enzyme, Idr, is involved in iodate respiration by *Pseudomonas* sp. *SCT*, 22, 2196–2212,  
927 <https://doi.org/10.1111/1462-2920.14988>, 2020.
- 928 Yu, Y., Chen, Y., Li, D., and Su, J.: A transient oxygen increase in the Mesoproterozoic ocean at ~1.44 Ga:  
929 Geochemical evidence from the Tieling Formation, North China Platform, *Precambrian Res.*, 369, 106527,  
930 <https://doi.org/10.1016/j.precamres.2021.106527>, 2022.
- 931 Zhang, S., Xu, C., Creeley, D., Ho, Y. F., Li, H. P., Grandbois, R., Schwehr, K. A., Kaplan, D. I., Yeager, C. M.,  
932 Wellman, D., and Santschi, P. H.: Response to comment on “iodine-129 and iodine-127 speciation in groundwater at  
933 hanford site, U.S.: Iodate incorporation into calcite,” *Environ. Sci. Technol.*, 47, 13205–13206,  
934 <https://doi.org/10.1021/es4046132>, 2013.
- 935 Zhou, X., Thomas, E., Rickaby, R. E. M., Winguth, A. M. E., and Lu, Z.: I/Ca evidence for upper ocean deoxygenation  
936 during the PETM, *Paleoceanography*, 29, 964–975, <https://doi.org/10.1002/2014PA002702>, 2014.
- 937 Zhou, X., Jenkyns, H. C., Owens, J. D., Junium, C. K., Zheng, X. Y., Sageman, B. B., Hardisty, D. S., Lyons, T. W.,  
938 Ridgwell, A., and Lu, Z.: Upper ocean oxygenation dynamics from I/Ca ratios during the Cenomanian-Turonian OAE  
939 2, *Paleoceanography*, 30, 510–526, <https://doi.org/10.1002/2014PA002741>, 2015.
- 940 Žic, V., Carić, M., and Ciglencečki, I.: The impact of natural water column mixing on iodine and nutrient speciation in  
941 a eutrophic anchialine pond (Rogoznica Lake, Croatia), *Estuar. Coast. Shelf Sci.*, 133, 260–272,  
942 <https://doi.org/10.1016/j.ecss.2013.09.008>, 2013.